Ocean Engineering 223 (2021) 108647

Contents lists available at ScienceDirect

Ocean Engineering

journal homepage: www.elsevier.com/locate/oceaneng

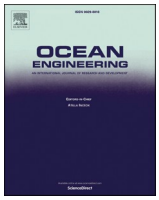

Numerical analysis on flow around a wall-mounted square structure using Dynamic Mode Decomposition

Guang Yin, Muk Chen Ong *

Department of Mechanical and Structural Engineering and Materials Science, University of Stavanger, Stavanger, Norway

ARTICLE INFO

Keywords:
Wall-mounted square structure
CFD
Turbulence
SADDES
Dynamic mode decomposition

ABSTRACT

Numerical investigations of the flow around a wall-mounted square structure have been carried out by using three-dimensional Spalart-Allmaras Delayed Detached Eddy Simulations (SADDES). The Reynolds number based on the free-stream velocity and the height of the structure is 1.19×10^5. The instantaneous hydrodynamic quantities are analyzed. The time-averaged results of the velocities, the Reynolds-averaged statistics and the vortical structures are presented and discussed. Dynamic Mode Decomposition (DMD) is applied to study the flow in the wake region behind the square structure. The dynamically important modes are extracted by further using a sparsity-promoted algorithm. The temporal information of the modes is compared with the results of the frequency analysis. The reduced order model of the flow field is constructed by the modes and shows good agreement with the numerical simulation results.

1. Introduction

Turbulent flows around wall-mounted structures commonly occur in many engineering problems. For instance, Glass-reinforced plastic (GRP) covers are used to protect the subsea installations, such as pipelines, from the potential damages caused by dropped objects and fishing gears. For the stable installation of the subsea covers, it is essential to obtain the hydrodynamic forces on them. The wall-mounted structures have also been used to enhance the heat transfer in gas turbines, combustion ducts and heat exchangers (Acharya et al., 1994; Hwang et al., 1999). Other applications can be found in protrusive devices on various transportations such as racing cars, aircrafts and ships (Dai et al., 2017). The flows around the wall-mounted structures display complex separation and reattachment features and induce complicate vortex arrangement in the separation region behind the structures. As a result, it is of great importance to study the flow characteristics around the structures. A common simplified model of these wall-mounted structures is a square cylinder lying on a flat wall, which is investigated in the present study.

Numerous studies have been conducted to study the flow around wall-mounted structures. Early studies include Arie et al. (1975), where experiments have been conducted to study the pressure distribution around square structures subjected to a turbulent boundary layer at Reynolds numbers of $3.4 \times 10^4 < Re < 1.19 \times 10^5$ (defined as $Re = U_\infty D/\nu$ where U_∞ is the free stream velocity and D is the height of the structure and ν is the kinematic viscosity of the fluid) and Tropea and Gackstatter (1985), where the experiments of the flow past a wall-mounted rectangular ribs were conducted in a channel at low Reynolds numbers of $150 < Re_h < 4500$ (defined based on the width of the channel). Experiments have also been performed by Martinuzzi et al. (1993) on the flows over square ribs with different spanwise lengths W/D of the structures (W is the spanwise length and D is the height of the structures of the ribs). It was found that the flow in the middle region of the wake behind the structures with $W/D > 6$ and the flow in front of the rib with $W/D > 10$ are essentially two-dimensional. Bergeles and Athanassiadis (1983) studied the recirculation length around a two-dimensional (2D) rectangular ribs using a single hot-wire and showed that the length of the recirculation region in front of the structures remains unchanged with the structure length while the length of the recirculation behind the structures varies linearly with the structure length. Liu et al. (2008) analyzed the spatio-temporal characteristics of the unsteady separation and reattachment of turbulent flows over a 2D square rib at $Re = 1.32 \times 10^4$ using experiments. The frequency features of the shedding large-scale vortex and the flapping separation bubbles were determined by the wall-pressure spectra. Despite experiments, numerical simulations were also adopted to study the turbulent boundary flow over wall-mounted structures. Hwang et al. (1999) employed 2D RANS (Reynolds-Averaged Navier-Stokes) simulations of the turbulent flow past a 2D rib with different length to height ratios

* Corresponding author.
E-mail address: muk.c.ong@uis.no (M.C. Ong).

https://doi.org/10.1016/j.oceaneng.2021.108647
Received 19 March 2020; Received in revised form 10 December 2020; Accepted 17 January 2021
Available online 5 February 2021

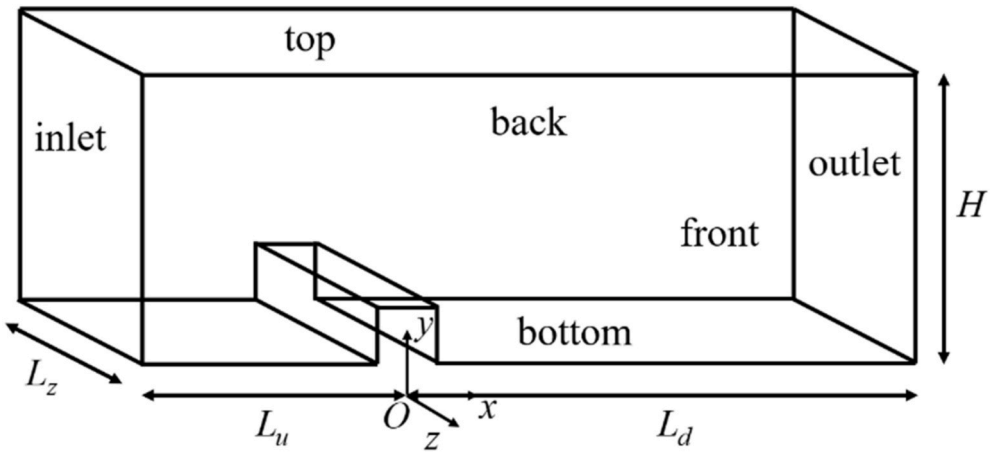

Fig. 1. Computational domain.

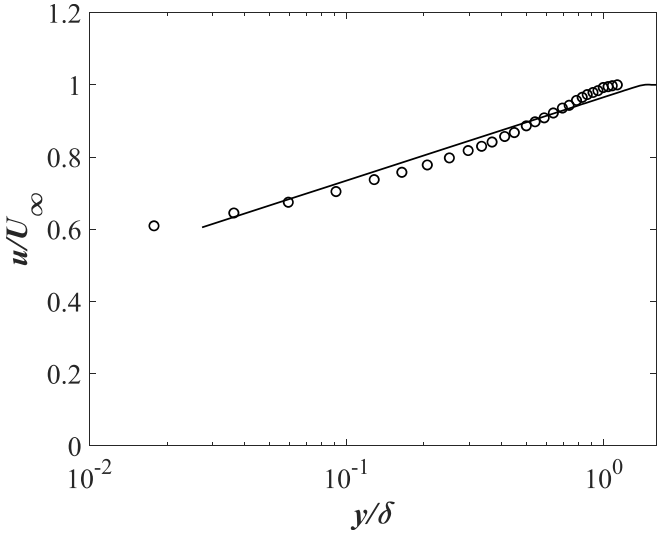

Fig. 2. The fitted logarithmic layer profile used in the present study (solid black line) compared with the experimental boundary layer profile reported by Arie et al. (1975) (circles).

Table 1
Results for different cases.

Case	L_z/D	Grids in XY plane	Grids in z direction	$\Delta t U_\infty/D$	C_D	C_L
1	4	55794	64	0.001	1.075	0.556
2	4	72433	64	0.001	1.079	0.541
3	4	93884	64	0.001	1.076	0.531
4	8	72433	128	0.001	1.087	0.554
5	4	55794	64	0.002	1.076	0.561
6	4	93884	96	0.001	1.068	0.529

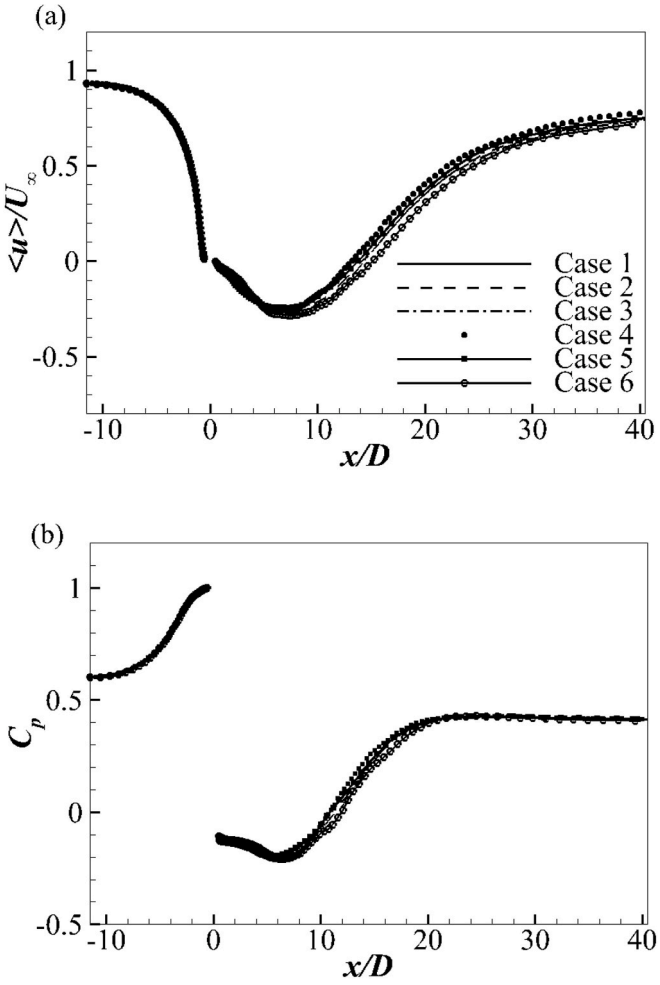

Fig. 3. Time- and spanwise-averaged streamwise velocity profiles $\langle u \rangle / U_\infty$ (a) and pressure coefficient profiles $\langle C_p \rangle$ (b) along x direction at $y = 0.5$.

using the standard $k-\varepsilon$ model. Acharya et al. (1994) used steady RANS simulations to predict the mean streamwise velocity and the turbulence intensity of the flow behind a wall-mounted 2D rib. Ryu et al. (2007) used RANS simulations based on the $k-\varepsilon$ model on the turbulent channel flow over 2D rib structures with different shapes to study the different drag forces and flow characteristics at $Re = 2 \times 10^4$.

The previous numerical simulations on the flow around 2D wall-mounted structures are largely carried out using the steady RANS since the wall can suppress the large-scale vortex shedding behind the structures. However, unsteady flow behaviors have been observed in the wake region behind the structures such as rolling-up of vortices and a flapping separation bubbles reported by Liu et al. (2008) which cannot be studied based on the steady RANS because only the time-averaged flow characteristics can be captured in the steady RANS simulations. Large Eddy Simulation (LES) was used to investigate the temporal behavior of the wake flow behind bluff bodies in various studies reported by Tian et al. (2014), Prsic et al. (2018) and Li et al. (2018).

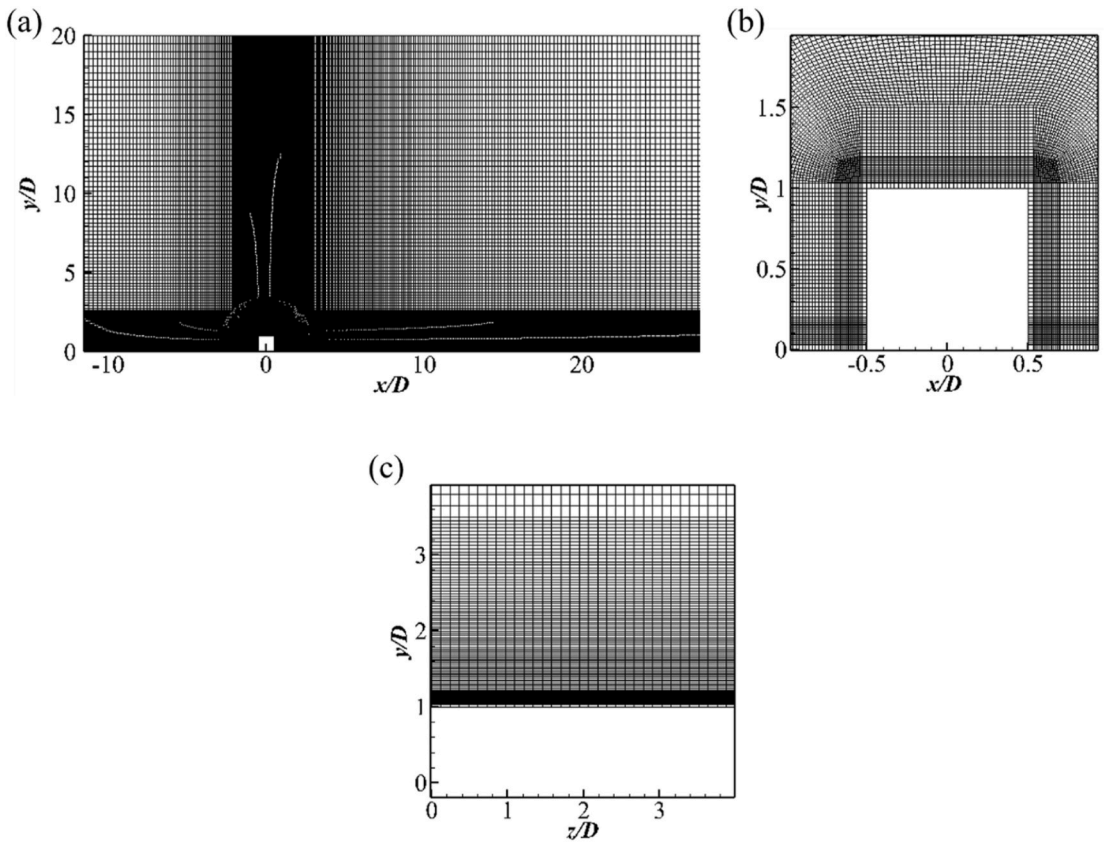

Fig. 4. An example of the meshes in the XY-plane of Case 5 in Table 1: (a) the whole computational domain, (b) grids around the structure and in the spanwise direction of YZ-plane (c) grids around the structure.

However, the computational cost of LES at high Reynolds numbers is high. Detached-eddy simulations (DES) proposed by Spalart et al. (1997) which is less computationally expensive, can be used for this purpose. The DES method is a combination of a RANS model in the attached boundary layer near the walls and a LES method in the separated regions away from the walls. An improvement to the standard DES (Spalart et al., 1997) was proposed by Spalart et al. (2006) known as delayed DES (DDES) to delay the switching from RANS to LES in the boundary layers. The method can prevent the artificial grid-induced separation (GIS). A detailed comparison was made by Boudreau et al. (2017) between the DDES simulation and URANS (unsteady RANS) simulation to show the ability of DDES in accurately capturing the wake behavior behind a square cylinder at $Re \tilde{} O(10^4)$. Furthermore, the DDES simulation was adopted by Ong et al. (2017) to study the flow structures around monopile and gravity-based wind turbine foundations at a high Reynolds number of $Re = 4 \times 10^6$. In the present study, 3D Spalart-Allmaras DDES (SADDES) method has been employed to investigate the unsteady flow in the wake region behind a wall-mounted square structures. To further understand the simulation results, the flow is analyzed using Dynamic Mode Decomposition (DMD) (Schmid 2010) to quantify the dynamical properties of the velocity fluctuations. The method was proposed based on the Koopman operator theory of dynamical systems (Rowley et al., 2009; Bagheri 2013). The dynamic information can be extracted from a time-resolved flow fields obtained by either numerical simulations (Schmid 2010; Tu et al., 2011; Zhang et al., 2017) or experimental data (Schmid 2011; Schmid et al., 2012; He et al., 2013; Seena and Sung, 2013; Tissot et al., 2013, 2014). The DMD method is regarded as an extension of the global stability analysis of a linear system. However, the explicit equations of the dynamical system are not required and it can be used as a data-driven method. For nonlinear systems such as the fully turbulence, a widely adopted method to extract important features is the proper orthogonal decomposition (POD) proposed by Lumely (1967). However, the POD modes are selected according to their energy and their temporal information is missing. The DMD method assumes that the temporal evolution of the dynamical system is governed by a linear operator, but it can still be applied to the nonlinear system and in fluid mechanics, it is used to extract the coherent structures from the flow fields.

The organization of the present paper is outlined as follows. The mathematical formulation and numerical methods are given in Section 2. The convergence studies and validation studies are presented in Section 3. The results and discussion in terms of hydrodynamics quantities, power spectra analysis of the fluctuations, instantaneous flow structures and DMD modes are given in Section 4. Finally, a conclusion is made for the present study.

2. Mathematical formulation and numerical method

2.1. Mathematical formulation

In the framework of DDES, the governing equations for the incompressible flow are filtered Navier-Stokes equations given as

$$\frac{\partial u_i}{\partial x_i} = 0 \tag{1}$$

$$\frac{\partial u_i}{\partial t} + \frac{\partial u_i u_j}{\partial x_j} = -\frac{\partial p}{\partial x_i} + \nu \frac{\partial^2 u_i}{\partial x_j \partial x_j} - \frac{\partial \langle u_i{}' u_j{}' \rangle}{\partial x_j} \tag{2}$$

where $i, j = 1, 2, 3$ (for x, y, z) is the streamwise, cross-stream and spanwise directions, respectively. u_1, u_2, u_3 (for u, v, w) are their corresponding resolved velocity components. $-\langle u_i{}' u_j{}' \rangle$ are the unresolved stresses, which are modeled by

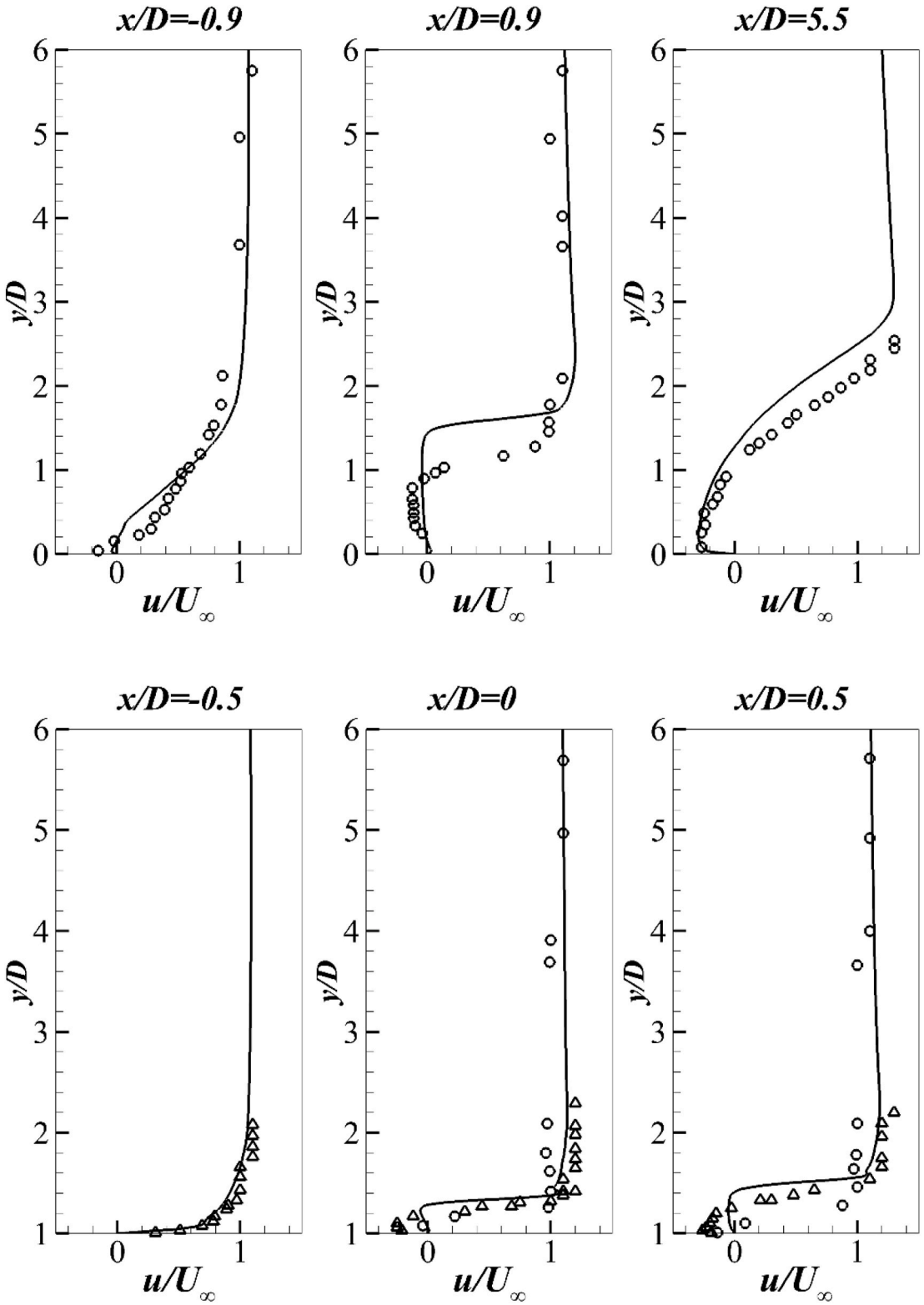

Fig. 5. Time- and spanwise-averaged streamwise velocity $\langle u\rangle/U_\infty$ (solid lines) at different streamwise locations compared with the experimental data reported by Acharya et al. (1994) (circles) and Crabb et al. (1977) (triangles).

$$-\langle u_i' u_j' \rangle = \nu_t \left(\frac{\partial u_i}{\partial x_j} + \frac{\partial u_j}{\partial x_i} \right) \tag{3}$$

An additional transport equation is used to calculate the modified viscosity $\widetilde{\nu}$ which can be found in Spalart et al. (2006) and is not described in detailed here. $\widetilde{\nu}$ is associated with the eddy viscosity ν_t as

$$\nu_t = \widetilde{\nu} f_{v1} f_{v1} = \frac{X^3}{X^3 + {C_{v1}}^3} X = \frac{\widetilde{\nu}}{\nu_t} \tag{4}$$

where $C_{v1} = 7.1$. In the present study, the f_{v3}-implementation (Rumsey et al., 2001) for the Spalart-Allmaras version is used to determine the

Table 2
Hit rates and fractional bias of the velocity profiles compared with the experimental data reported by Acharya et al. (1994) and Crabb et al. (1977).

Locations	Hit rate q	Fractional bias (FB)
$x/D = -0.9$	0.684	0.03526
$x/D = 0.9$	0.4	0.3084
$x/D = 5.5$	0.24	0.7179
$x/D = -0.5$	0.867	0.0829
$x/D = 0$	0.818	0.0612
$x/D = 0.5$	0.67	0.1342

terms in the transport equation of $\widetilde{\nu}$.

In the original DES formulation, the distance between a point in the flow domain and the wall d in the destruction term of the viscosity transport equation is modified as

$$\widetilde{d} = min(d, C_{DES}\Delta) \tag{5}$$

where $C_{DES} = 0.65$ is a constant and Δ is the length scale associated with the local grid spacings in the three directions:

$$\Delta = max(\Delta_x, \Delta_y, \Delta_z) \tag{6}$$

DDES is proposed to overcome the issue of "grid-induced separation" (GIS) by delaying the transition from RANS in the attached boundary layer region to LES in the separation region away from the wall. In this method, $\widetilde{d}$ is modified as

$$\widetilde{d} = d - f_d max(0, d - C_{DES}\Delta) \tag{7}$$

where f_d is a filter function designed to be 0 in the RANS region and 1 in the LES region.

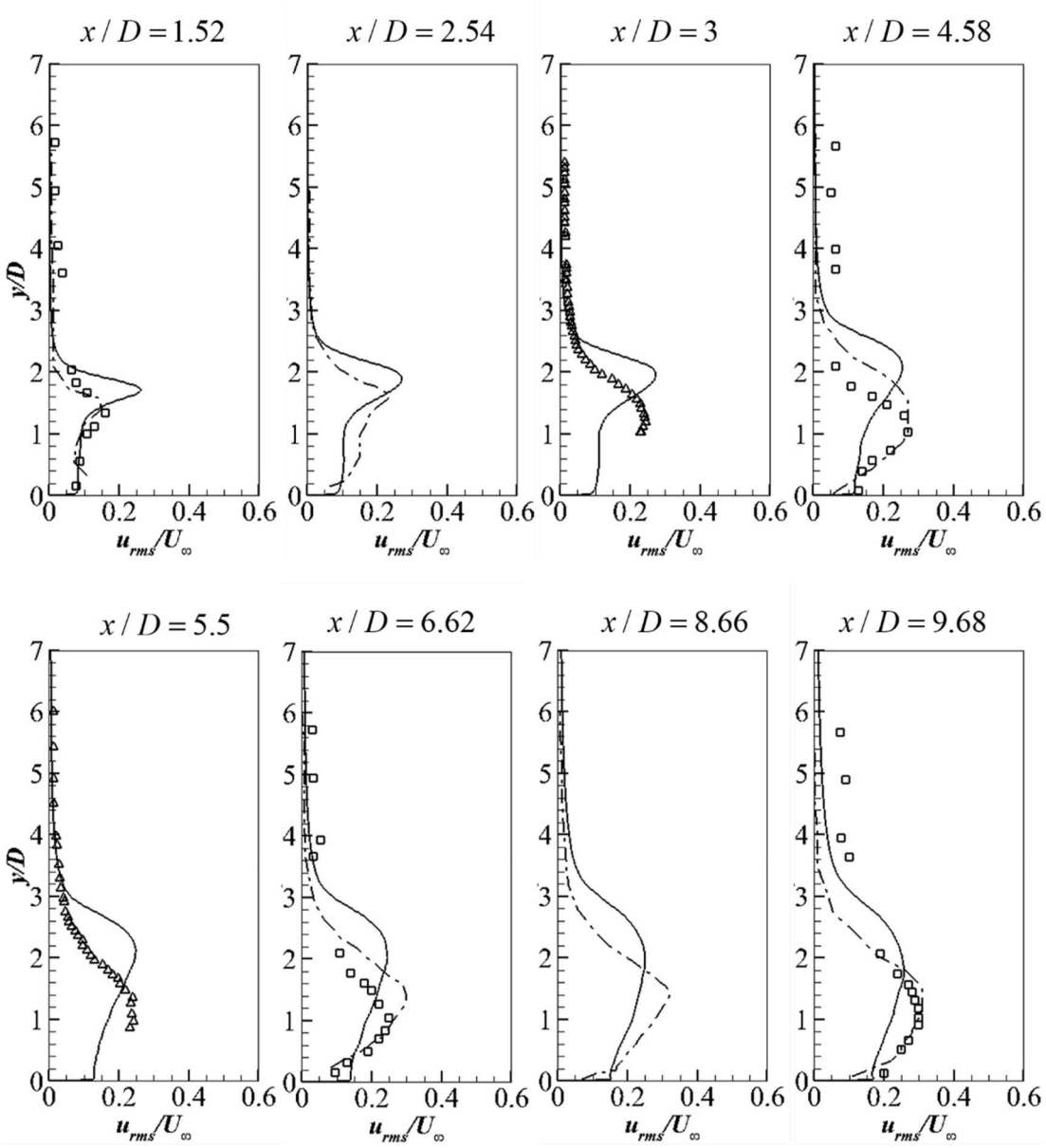

Fig. 6. Time- and spanwise-averaged u_{rms}/U_∞ (solid lines) at different streamwise locations compared with the LES results obtained by Gu et al. (2017) (dash-dotted lines) and experimental data reported by Acharya et al. (1994) (squares) and Tariq et al. (2004) (triangles).

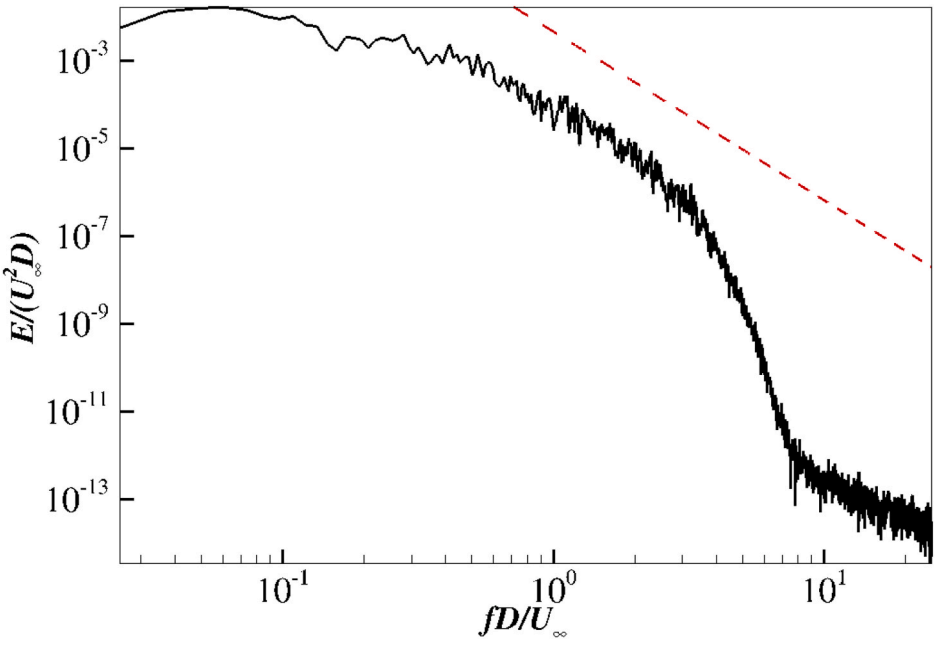

Fig. 7. Energy spectra of the resolved cross-stream velocity fluctuations at the mid-span point of $(x/D, y/D, z/D) = (1, 0.5, 2)$ compared with the $-5/3$ law (red dashed line). (For interpretation of the references to color in this figure legend, the reader is referred to the Web version of this article.)

2.2. Numerical methods

OpenFOAM, an open source Computational Fluid Dynamic (CFD) code, is used in the present study. The PISO (Pressure Implicit with Splitting of Operators) scheme is used. The spatial schemes for gradient, Laplacian and divergence are Gauss linear, bounded Gauss linear upwind, and Gauss linear limited corrected, respectively.

3. Computational overview

3.1. Computational domain

The computational domain is shown in Fig. 1. The origin of the coordinates is located at the center of the bottom edge of the wall-mounted square structures. The length and height of the computational domain are $50D$ and $20D$, respectively. The spanwise length L_z will be determined in the next section. The distance between the inlet boundary and the center of the bottom edge of the square structure is set to be $Lu = 11.5D$ and the distance between the outlet boundary and the center of the bottom edge of the structure is set to be $Ld = 40.5D$. This inlet length is larger than that used in Ong et al. (2010) where numerical simulations were carried out for the flow around a cylinder close to a flat wall at $Re = 3.6 \times 10^6$ with an inlet length of $10D$. The outlet length is also larger than that used in the previous similar numerical studies such as Young et al. (2006) at with $Ld = 20D$, Ong et al. (2009, 2010) at $Re \sim O(10^6)$ with $Ld = 20D$, Tian et al. (2014) at $Re = 1.5 \times 10^5$ with $Ld = 20D$ and Tian et al. (2016) at $Re = 1.5 \times 10^5$ with $Ld = 15D$. Based on these studies, the size of the domain in the XY plane is large enough to suppress any far field effects. The boundary conditions for the simulations are set as follows:

(1) A seabed boundary layer flow with a logarithmic horizontal velocity profile is used at the inlet boundary in x direction. The logarithmic velocity profile with a boundary layer thickness of $\delta = 0.73D$ is adapted by curve fitting of the boundary layer profile obtained in the experiments done by Arie et al. (1975). The obtained velocity profile is shown in Fig. 2 compared with the experimental velocity profile reported by Arie et al. (1975). The velocity in y and z direction is set to be zero.

The inlet turbulent quantities are prescribed by implementing the turbulent viscosity which is given by

$$\nu_t = C_\mu k^2/\varepsilon \tag{8}$$

using the definition in the $k-\varepsilon$ model with $C_\mu = 0.09$. The turbulent kinetic energy k and the rate of dissipation of turbulent kinetic energy ε are given by

$$k = \begin{cases} \max\left\{C_\mu^{-1/2}(1-z/\delta)^2 u_\tau^2, 0.0001U_\infty^2\right\}, \text{if } z \le \delta \\ 0.0001U_\infty^2, \text{if } z > \delta \end{cases} \tag{9}$$

$$\varepsilon = \left(C_\mu^{3/4} k^{3/2}\right)/l \tag{10}$$

where the turbulent length scale l is given by $l = \min\{\kappa y(1+3.5y/\delta)^{-1}, C_\mu\delta\}$ with $\kappa = 0.41$. The same method for prescribing the turbulent viscosity has also been used Ong et al. (2017) where Spalart-Allmaras DDES model was also adopted.

(2) No-slip condition ($u = v = w = 0$) is applied on the bottom and the surface of the square structure. The pressure is set to be zero normal gradient. In the present study, the flow around the square surface is fully developed turbulent and a wall function based on the Spalding's law of the wall (Spalding 1961) is applied for the near-wall region.
(3) At the outlet and top boundaries, the velocities, pressure and ν_t are set as zero normal gradient.
(4) The periodic boundary conditions are used for all the variables on the two XY planes in the spanwise directions.

A parallel computing technique is used for the simulations on a distributed memory system in a Notur project and the computational domain is divided into 128 or 256 subdomains based on different cell numbers.

3.2. Convergence studies

Convergence studies are carried out to determine the spanwise length, the grid and time resolutions of the simulations. The parameters

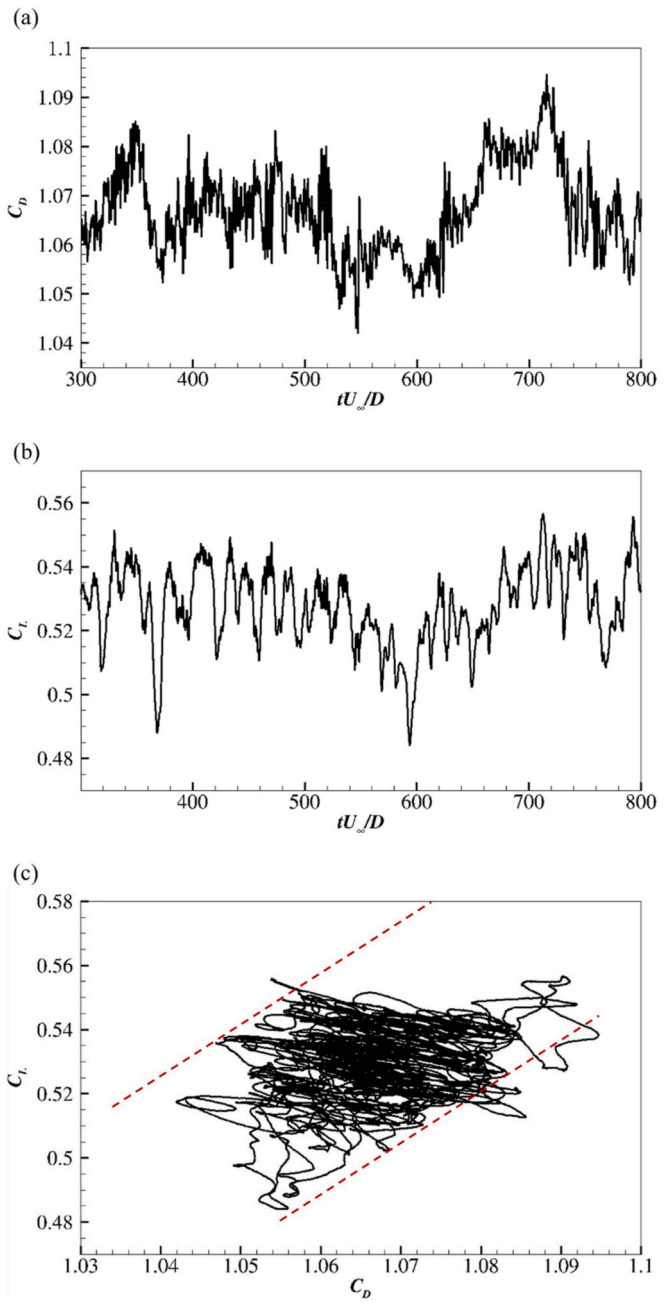

Fig. 8. Time histories of (a) C_D; (b) C_L; (c) the phase-space plot of the two quantities.

and the results are shown in Table 1. Δt is the time step and all the simulations are run for a non-dimensional time of $1000D/U_\infty$ (U_∞ is the free stream velocity and a total computational time in a range of 38400–128000 CPU hours is used for each case). The time-averaged drag coefficients and lift coefficients of different cases are considered, which are defined as follows:

$$\langle C_D \rangle = \frac{\langle F_x \rangle}{\frac{1}{2}\rho U_\infty^2 D L_z} \tag{11}$$

$$\langle C_L \rangle = \frac{\langle F_y \rangle}{\frac{1}{2}\rho U_\infty^2 D L_z} \tag{12}$$

where F_x is the total force obtained by integrating the pressure and the shear stress acting on the surfaces of the square structure in x direction and F_y is the force in y direction.

First, results of Case 1∼Case 3 with different grids numbers in XY plane and the same L_z, grids number in z direction and Δt show that there is no significant difference in $\langle C_D \rangle$ and the relative difference among $\langle C_L \rangle$ of the three cases are within 4.7%. Then, $\langle C_D \rangle$ and $\langle C_L \rangle$ of Case 2 and Case 4 with different L_z and the same grid resolution in z direction shows that when increasing L_z from 4 to 8, the relative difference between $\langle C_D \rangle$ is within 1% while the relative difference between $\langle C_L \rangle$ is 4.3%, indicating that $L_z = 4$ is enough to provide converged results and this value is adopted for the other simulations. The relative difference between $\langle C_D \rangle$ of Case 1 and Case 5 with different Δt is less than 1% and the relative difference between $\langle C_L \rangle$ is within 2%. Therefore, $\Delta t = 0.001$ is used for all the rest simulations in the present study. It worth mentioning that the minimal Taylor time scale defined as $\tau_\lambda = (15\nu/\varepsilon)^{1/2}$ of the present study is calculated to be 0.04 and the time step of $\Delta t = 0.001$ is much smaller than the minimal Taylor time scale, and hence also smaller than the large eddy scales. With a finer grid resolution in z direction for Case 6, both $\langle C_D \rangle$ and $\langle C_L \rangle$ decrease compared with Case 3. However, the relative differences for Case 6 from Case 3 is within 1% and 2% for the two quantities.

Furthermore, the time- and spanwise-averaged streamwise velocity $\langle u \rangle / U_\infty$ and the pressure coefficient $\langle C_p \rangle$ (defined as $2(\langle p \rangle - p_\infty)/(\rho U_\infty^2)$ where p_∞ is chosen such that $\langle C_p \rangle$ at the front stagnation point on the front face of the structure is unity) along the streamwise direction at $y = 0.5$ are compared among different cases as shown in Fig. 3. It is shown that the results agree well with each other which indicate that the grid and time-step convergences have been achieved. Fig. 4 shows an example of the meshes of Case 5 in Table 1 in the XY-plane and the YZ-plane.

3.3. Validation studies

Validation studies are conducted by comparing the converged results of Case 6 in Table 1 with the published data. The $\langle C_D \rangle$ value of Case 6 is in satisfactory agreement with the experimental data of $\langle C_D \rangle = 0.96$ reported by Arie et al. (1975) with a relative difference of 10.8% and the numerical data of $C_D = 1.02$ obtained by 2D RANS simulation reported by Tauqeer et al. (2017) with a relative difference of 5.2%.

Further validation studies are done by comparing $\langle u \rangle / U_\infty$ at different streamwise locations of $x/D = -0.9, 0.9, 5.5$ and $x/D = -0.5, 0, 0.5$ on the top of the square with the experimental data in turbulent channel flows reported by Crabb et al. (1977) as well as Acharya et al. (1994) in Fig. 5. The comparison shows that the results of the present study are overall in good agreement with the experimental data except that there is a discrepancy at $x/D = 0.9$ and $x/D = 5.5$ in the wake region where adverse pressure gradient takes place. Furthermore, the hit rates and fractional bias of the present predicted time- and spanwise-averaged velocity profiles compared with the experimental data are at these locations are presented in Table 2. According to Santiago et al. (2007), the hit rate value q and the fractional bias value (FB) for the velocity profile at each location are defined as

$$q = \frac{1}{n}\sum_{i=1}^{n} N_i \; with \; N_i = \begin{cases} 1, \text{if} |P_i - O_i|/|O_i| \le RD \;\; \text{or} \;\; |P_i - O_i| \le AD \\ 0, \text{else} \end{cases} \tag{13}$$

$$\text{FB} = \left(\overline{O} - \overline{P}\right) \Big/ 0.5\left(\overline{P} + \overline{O}\right) \tag{14}$$

where n is the total number of points at each locations in Fig. 3. The values of P_i and O_i denote the present predicted data and the experimental data, respectively; $\overline{P}$ and $\overline{O}$ denote their mean values. RD and AD denotes a relative and absolute deviations, respectively. As suggested by Santiago et al. (2007), the values of $RD = 0.25$ and $AD = 0.05$ are used. It can be seen that close to the square structure, the velocity profiles can fulfil the criterion of $q \ge 66\%$ as proposed by Schlünzen et al. (2004). Far away downstream the square structure, the hit rates can be large. In

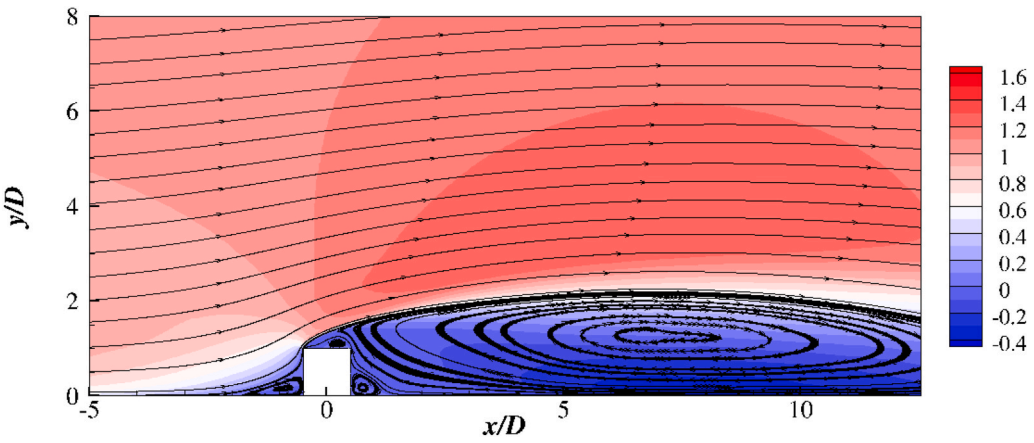

Fig. 9. The contours of the streamwise velocity $\langle u\rangle/U_\infty$ and streamlines of the time- and spanwise-averaged flow.

addition, the present simulation tends to underestimate the streamwise time- and spanwise-averaged velocity based on the FB values.

Fig. 6 shows profiles of the spanwise-averaged u_{rms}/U_∞ at different streamwise locations of the present study are compared with the previous published experimental data reported by Acharya et al. (1994) and Tariq et al. (2004) and LES results reported by Gu et al. (2017). It can be seen that the values of u_{rms}/U_∞ are in general comparable to the published data. However, the wall-normal locations of the peak value of u_{rms}/U_∞ are overpredicted for the present study and the discrepancy can be attributed to the higher Re of the present study compared with those used in the previous studies.

Finally, the energy spectra of the resolved cross-stream velocity fluctuations obtained at the location of $(x/D, y/D, z/D) = (1,\ 0.5, 2)$ of Case 6 in the wake region behind the square is shown in Fig. 7. It can be seen that the inertial subrange of the energy spectra follows well with the Kolmogorov spectra with a $-5/3$ slope, which confirms the validity of the present turbulence modeling.

4. Results and discussion

4.1. Hydrodynamic forces

The hydrodynamics forces are analyzed in this section in terms of the instantaneous drag force and lift force acting on the square structure. The time histories of C_D and C_L are shown in Fig. 8 (a) and (b). It is obvious that the frequency of C_L is lower than that of C_D. There are clearly high and low drag regimes in C_D which is closely related to the high and low C_L. The approximate positive correlation between the instantaneous values of two force coefficients is also observed in the phase-space plot of C_D and C_L as shown in Fig. 8 (c), where the envelop of C_L is amplified by C_D. This behavior has also been reported in Najjar and Balachandar (1998), Tian et al. (2014) and Hemmati et al. (2019). However, due to the presence of the bottom flat wall, the linear increase of C_L with C_D is not as apparent as that of the flow around a flat plate reported by Tian et al. (2014).

4.2. Reynolds-averaged statistics and instantaneous flow visualizations

Reynolds-averaged statistical quantities are discussed in this section. Fig. 9 shows the streamlines of the time- and spanwise-averaged flows of Case 6. There are three main recirculation motions around the square, which are also reported by Tauqueer et al. (2017). A small one is formed around the front face of the structure and a large recirculation motion is generated due to the separation of the shear layer behind the square. The third smaller one is induced by the large recirculation vortex around the rear face of the square. On the top of the square, a secondary separation appears which causes an additional small vortex. This is also observed on the top of a flat plate reported by Tian et al. (2014).

The contours of resolved Reynolds stresses $\langle u'u'\rangle/U_\infty^2$, $\langle v'v'\rangle/U_\infty^2$, $\langle u'v'\rangle/U_\infty^2$ are presented in Fig. 10. Due to the DDES used in the present study, the Reynolds stresses are low near the surface of the square where RANS equations are solved. High levels of the three Reynolds stresses are all located around the shear layer behind the square. The peak value of $\langle u'u'\rangle/U_\infty^2$ is located downstream at $x/D \approx 3$ while the peak value of $\langle v'v'\rangle/U_\infty^2$ is located closer to the square at $x/D \approx 0.5$. The peak value of $\langle u'v'\rangle/U_\infty^2$ is located between the peak locations of the other two quantities.

Fig. 11 shows the instantaneous 3D vortical structures at $t = 800D/U_\infty$ identified by the Q criterion defined by

$$\mathrm{Q} = \frac{1}{2}\left(\boldsymbol{\Omega}^2 - \boldsymbol{S}^2\right) \tag{15}$$

where $\boldsymbol{S}$ and $\boldsymbol{\Omega}$ is the strain and the rotation tensor, respectively. The isosurfaces of nondimensionalized $QD/U_\infty = 2.5$ are colored by the time-averaged streamwise velocity. A shear layer is formed after the separation point and are shed due to the shear-layer instability as marked as 'S'. The shear layer begins to rolling-up (denoted as 'R') into hairpin vortices (denoted as 'H') and they are becoming larger further downstream. Due to the high Re, the vortical structures are highly three-dimensional and spatially irregular. The vortical structures gathering around the shear layer are mostly in the spanwise direction while those in the wake region tend to be in the streamwise direction.

4.3. Dynamical mode decomposition analysis

In this section, the DMD method is employed to analyze the dynamical properties of the flow. The algorithm of DMD can be briefly outlined as follows. The input datasets in the form of a sequence of snapshots are denoted as two matrices

$$\boldsymbol{V}_1^N = [v_1, v_2, v_3, \ldots v_N] \in R^{N_x \times N} \tag{16}$$

$$\boldsymbol{V}_2^N = [v_2, v_3, v_4, \ldots v_{N+1}] \in R^{N_x \times N} \tag{17}$$

and a column vector v_i $(i = 1, 2, 3 \ldots N)$ denotes the input data at time step of $t = t_i$, which is usually the velocities or the pressure stored at every nodes in the flow field. N_x denotes the total number of the measured signals at all observation nodes in the experiments or numerical simulations. The time step between two snapshots is Δt. In the DMD method, it is assumed that the there is a linear operator $\boldsymbol{A}$ between two consecutive snapshots $v_{i+1} = \boldsymbol{A}v_i$ and the relationship between the two data sequence matrices can be written as

$$\boldsymbol{A}\boldsymbol{V}_1^N = \boldsymbol{V}_2^N \tag{18}$$

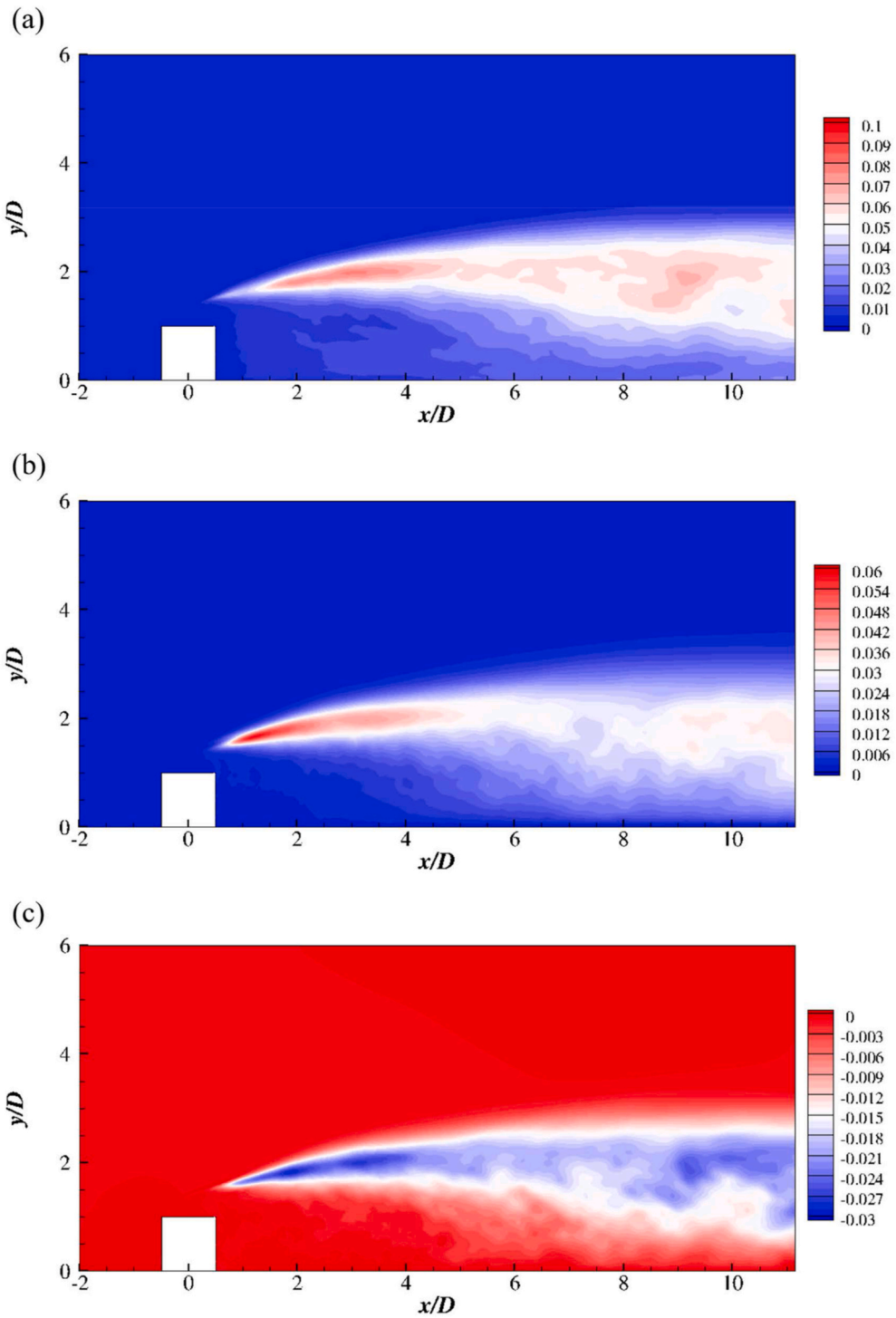

Fig. 10. Contours of resolved Reynolds stresses. (a) The streamwise normal stress $\langle u'u' \rangle / U_\infty^2$; (b) The cross-stream normal stress $\langle v'v' \rangle / U_\infty^2$; (c) The shear stress $\langle u'v' \rangle / U_\infty^2$.

The DMD method aims to determine eigenvalues and eigenvectors of the unknown operator $\boldsymbol{A}$. The eigenvalues of the operator can describe the dynamical properties inherited in the data sequence. For a fluid mechanic problem, the number of the components of each vector v_i, N_x is usually larger than the total number of the snapshots N and the DMD method can provide a reduced-order representation of the linear operator $\boldsymbol{A}$. First, the singular value decomposition (SVD) is applied for the matrix $\boldsymbol{V}_1^N$

$$\boldsymbol{V}_1^N = \boldsymbol{U}\boldsymbol{\Sigma}\boldsymbol{V}^T \tag{19}$$

where $\boldsymbol{\Sigma}$ is an diagonal matrix contain non-zero singular values on its diagonal. $\boldsymbol{U}$ and $\boldsymbol{V}$ contain orthogonal unit columns ($\boldsymbol{U} \in R^{N_x \times N}$ and $\boldsymbol{V} \in R^{N \times N}$ and $\boldsymbol{U}^T\boldsymbol{U} = \boldsymbol{I}\,\boldsymbol{V}^T\boldsymbol{V} = \boldsymbol{I}$, where "$T$" denotes the transpose of the matrix) and the column vectors of $\boldsymbol{U}$ are usually denoted as the proper orthogonal decomposition (POD) modes of the data sequence $\boldsymbol{V}_1^N$. Then, the linear mapping relationship of $\boldsymbol{V}_1^N$ and $\boldsymbol{V}_2^N$ can be expressed as

$$\boldsymbol{V}_2^N = \boldsymbol{A}\boldsymbol{U}\boldsymbol{\Sigma}\boldsymbol{V}^T \tag{20}$$

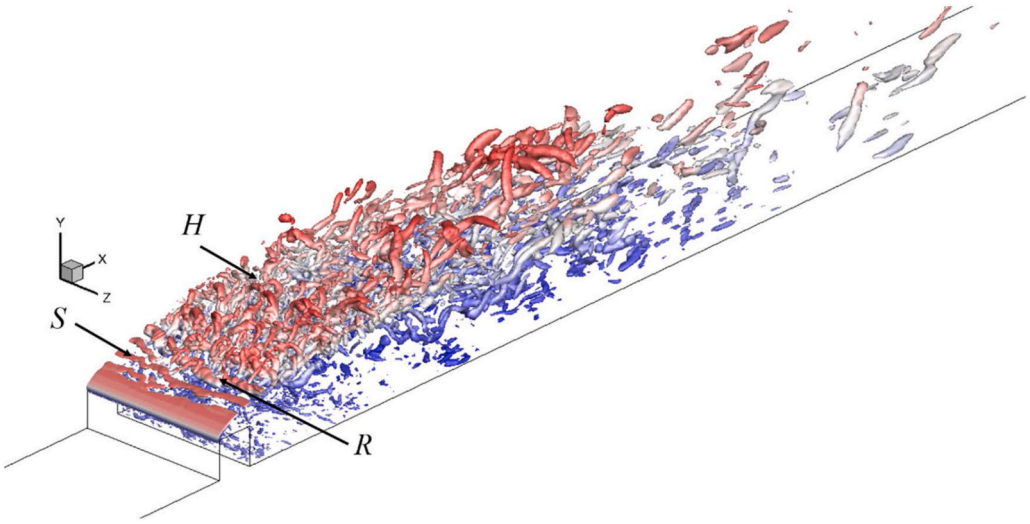

Fig. 11. Instantaneous iso-surface of $QD/U_\infty = 2.5$ at $tU_\infty/D = 800$ colored by the time- and spanwise-averaged streamwise velocity $\langle u \rangle / U_\infty$.

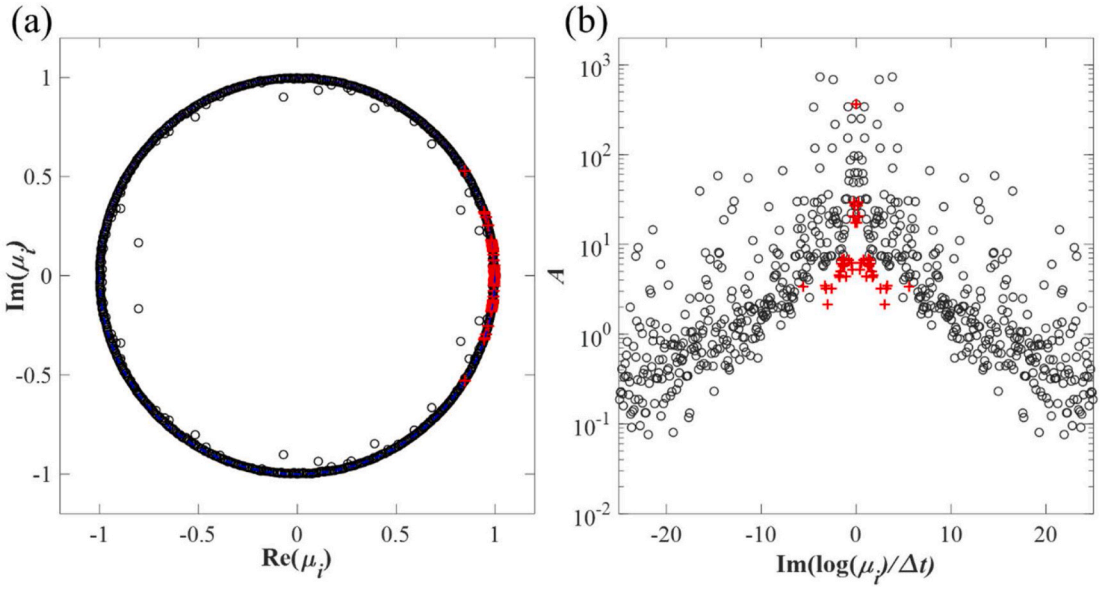

Fig. 12. (a). DMD eigenvalues; (b). DMD spectrum (black circles: obtained by Eq. (17), and red crosses: selected by the SPDMD algorithm). (For interpretation of the references to color in this figure legend, the reader is referred to the Web version of this article.)

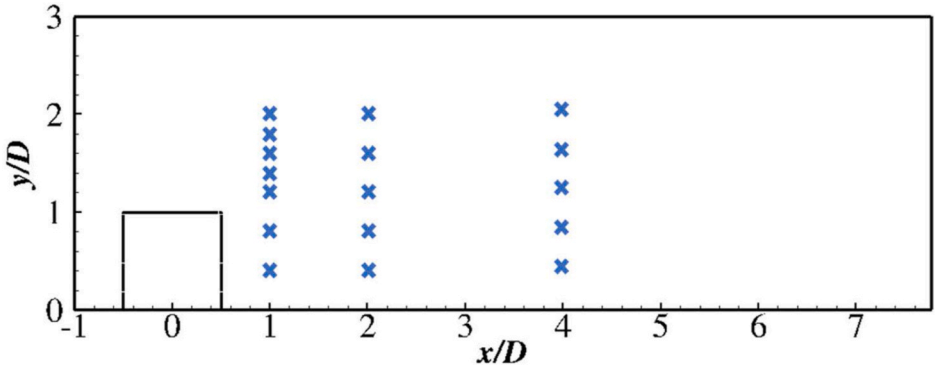

Fig. 13. Locations of probes for PSD analysis.

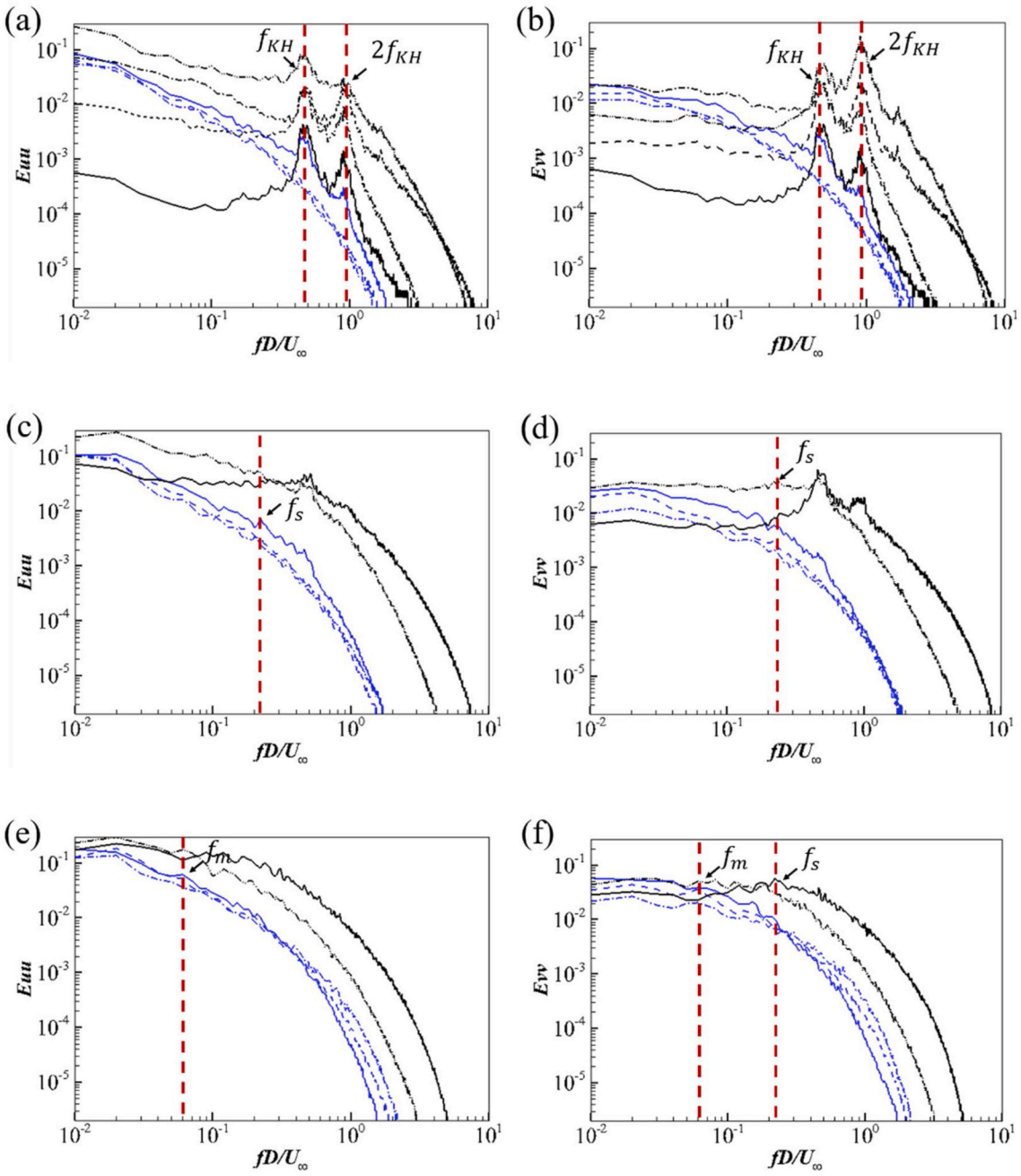

Fig. 14. The power spectral densities (PSDs) of the streamwise velocity at (a) $x/D = 1$; (c) $x/D = 2$; (e) $x/D = 4$ and the cross-stream velocity at (b) $x/D = 1$; (d) $x/D = 2$; (f) $x/D = 4$. (Blue solid: $y/D = 0.4$; Blue dashed: $y/D = 0.8$; Blue dash-dotted: $y/D = 1.2$; Black dashed: $y/D = 1.4$; Black solid: $y/D = 1.6$; Black dotted: $y/D = 1.8$; Black dash-dot-dotted: $y/D = 2.0$). (For interpretation of the references to color in this figure legend, the reader is referred to the Web version of this article.)

and the reduced-order representation of $\boldsymbol{A}$ can be obtained by projecting $\boldsymbol{A}$ on $\boldsymbol{U}$ as

$$\widetilde{\boldsymbol{A}} = \boldsymbol{U}^T\boldsymbol{A}\boldsymbol{U} = \boldsymbol{U}^T\boldsymbol{V}_2^N\boldsymbol{V}\boldsymbol{\Sigma}^{-1} \tag{21}$$

Because of the orthogonality of the column vector of $\boldsymbol{U}$, the matrix $\widetilde{\boldsymbol{A}}$ with a lower dimension of $N \times N$ contains the same eigenvalues as $\boldsymbol{A}$ with the dimension of $N_x \times N_x$. By solving the eigenvalue problem

$$\widetilde{\boldsymbol{A}}\boldsymbol{Y} = \boldsymbol{Y}\boldsymbol{\Lambda} \tag{22}$$

the eigenvalue of $\boldsymbol{A}$ can be obtained as $\boldsymbol{\Lambda} = \mathbf{diag}(\boldsymbol{\mu}_1, \boldsymbol{\mu}_2, \ldots \boldsymbol{\mu}_N)$and their corresponding eigenmodes are obtained by $\boldsymbol{\Phi} = \boldsymbol{U}\boldsymbol{Y} = [\boldsymbol{\varphi}_1, \boldsymbol{\varphi}_2, \boldsymbol{\varphi}_3 \ldots, \boldsymbol{\varphi}_N]$, which are also denoted as the DMD modes. According to Schmid (2010), $\mathrm{Im}(\log(\mu_i)/\Delta t)$ represents the frequency and $\mathrm{Re}(\log(\mu_i)/\Delta t)$ represents the amplification rate of the mode.

An important question in the DMD method is to determine a small subset of DMD modes that can provide a reduced order approximation of the dynamic system represented by the data sequence (16). Different from the POD modes whose contributions to the data sequence are ranked according to their energy levels, the contribution of each DMD mode is difficult to measure because no information of their energy can be obtained through the algorithm. A sparsity-promoting (SP) DMD (SPDMD) method is proposed by Jovanović et al. (2014) to select a subset of dynamically important modes. This algorithm was further improved and adopted to analyze the flow past a circular cylinder at low *Re* in Ohmiche (2017). Given the DMD modes $\boldsymbol{\varphi}_i$ and their eigenvalues

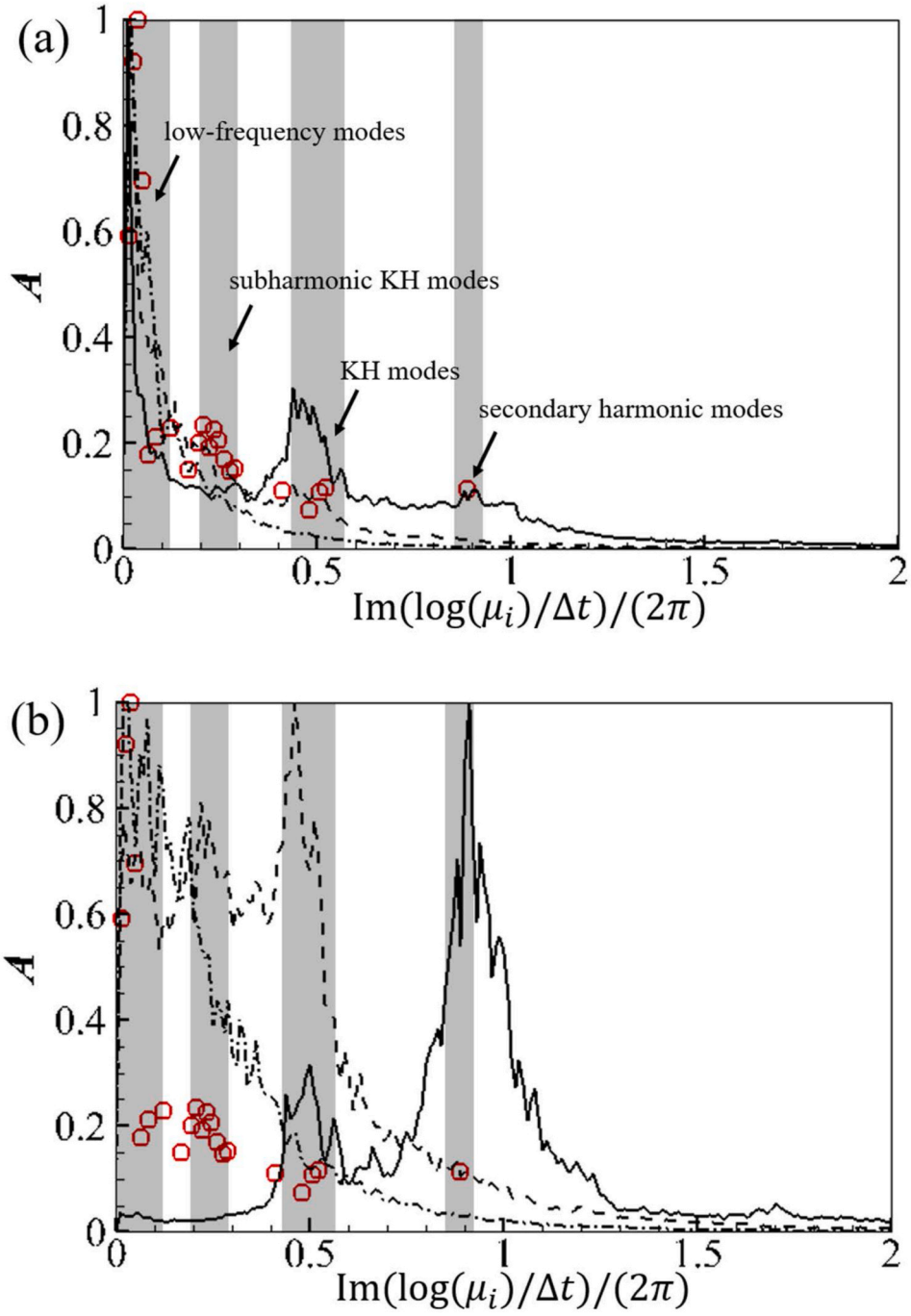

Fig. 15. The DMD spectrum (red circles) obtained by the SPDMD algorithm and the power spectral densities (PSDs) of the streamwise velocity (a) and the cross-stream velocity (b) at $x/D = 1$ (solid); $x/D = 2$ (dashed); $x/D = 4$ (dash-dotted). (For interpretation of the references to color in this figure legend, the reader is referred to the Web version of this article.)

$\boldsymbol{\mu}_i$, the input dataset can be approximated as

$$\boldsymbol{V}_1^N \approx \boldsymbol{\Phi}\boldsymbol{D}_{\boldsymbol{\alpha}}\boldsymbol{V}_{\mathbf{and}} = [\boldsymbol{\varphi}_1, \boldsymbol{\varphi}_2, \boldsymbol{\varphi}_3 \ldots, \boldsymbol{\varphi}_N] \begin{bmatrix} \boldsymbol{\alpha}_1 & & \\ & \cdots & \\ & & \boldsymbol{\alpha}_N \end{bmatrix} \begin{bmatrix} \boldsymbol{\mu}_1^0 & \cdots & \boldsymbol{\mu}_1^{N-1} \\ \vdots & \ddots & \vdots \\ \boldsymbol{\mu}_N^0 & \cdots & \boldsymbol{\mu}_N^{N-1} \end{bmatrix} \tag{23}$$

where $\boldsymbol{D}_{\boldsymbol{\alpha}} = \mathbf{diag}(\boldsymbol{\alpha}_1, \ldots, \boldsymbol{\alpha}_N)$ denote the amplitudes of their corresponding DMD modes within the time span. The amplitude of each DMD mode $\boldsymbol{\alpha}_i (i = 1, 2, 3 \ldots N)$ is regarded as the measurement of its contribution to the dynamic system. $\boldsymbol{V}_{\mathbf{and}}$ denotes the Vandermonde matrix contained the temporal variations of each mode during the time span.

By introducing a penalty function γ, an optimization problem is solved to determine the unknown amplitudes matrix $\boldsymbol{D}_{\boldsymbol{\alpha}}$

$$\min_{\boldsymbol{\alpha}} \left\| \boldsymbol{V}_1^N - \boldsymbol{\Phi}\boldsymbol{D}_{\boldsymbol{\alpha}}\boldsymbol{V}_{\mathbf{and}} \right\|_F^2 + \gamma \sum_{i=1}^{N} |\boldsymbol{\alpha}_i| \tag{24}$$

$\|\ldots\|_F$ is the Frobenius norm of a matrix. According to Jovanović et al. (2014), the positive parameter γ is choose to achieve a balance between the accuracy of the approximation (24) and the number of efficient DMD modes used in the approximation, i.e. the sparsity of the amplitude matrix $\boldsymbol{D}_{\boldsymbol{\alpha}}$. For a large γ, most of the element in $[\boldsymbol{\alpha}_1, \ldots, \boldsymbol{\alpha}_N]$ becomes 0. It means that the SPDMD method removes the modes which only influence

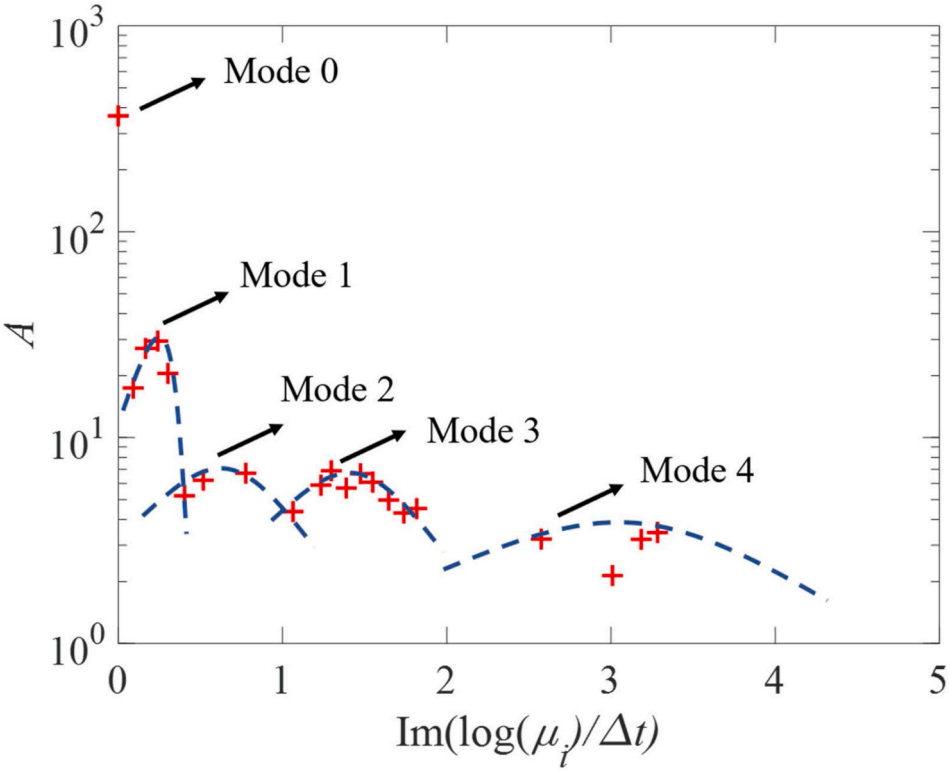

Fig. 16. DMD spectrum selected by SPDMD with 4 clusters.

the early stages of the time evolution and are damped quickly as well as the modes with small amplitudes. Hence, the DMD modes with non-zero elements in $[\boldsymbol{\alpha}_1, \ldots, \boldsymbol{\alpha}_N]$ which contribute the most to the dynamic system are kept.

In the present study, the SPDMD algorithm is performed on the (u, v) data obtained in the 2D XY-plane at the mid-span point $z = 0$ of the computational domain. The similar 2D (two-dimensional)-2C (two-components) DMD analysis was also performed by Tissot et al. (2013) on the flow around a cylinder. The number of the snapshots is $N = 800$ from the time span of $450 \leq tD/U_\infty \leq 530$ with a time step of $\Delta tD/U_\infty = 0.1$. The DMD eigenvalues obtained by (22) are shown in Fig. 12 (a) together with a subset of eigenvalues corresponding to the $N_{sp} = 57$ modes selected by the SPDMD algorithm. and the others are located inside the unit circle. When the eigenvalue of a DMD mode is located on the unit circle, the growth/decay rate of the mode is zero and the mode is 'neutrally stable' as described in Schmid et al. (2010), Schmid (2011) and Pan et al. (2015). It can be seen from Fig. 12 (a) that most of the eigenvalues lies on the unit circle due to the statistically stationary state of the turbulent flow. This behavior has also been widely reported in Seena and Sung (2011), Statnikov et al. (2015) and Wu et al. (2019). Other modes are located inside the unit circle and they have negative growth rates. These modes are strongly damped within the temporal evolution of the dynamical system as reported in Jovanović et al. (2014). The power spectrum of the DMD modes obtained by (22) as well as the modes selected by SPDMD are shown in Fig. 12 (b). It can be seen that after the SPDMD algorithm is applied, most of the modes are removed because even though they have large amplitudes, they are damped quickly during the time evolution. The modes with lower frequencies are left which make the most contribution to the dynamical system. Among the remaining modes after the SPDMD algorithm, the most dominant mode corresponds to the time-averaged flow with a frequency of 0. All the other frequencies correspond to the turbulent fluctuations which appear in pair. The DMD spectrum with the frequencies $\mathrm{Im}(\log(\mu_i)/\Delta t) > 0$ of the remaining modes are shown in Fig. 15. All the spectrum is widely distributed since the flow is fully developed turbulence which displays multi-scale features. However, all the spectrum is observed to cluster around 4 peaks as indicated in Fig. 16. A comparison between the DMD spectrum and the power spectral densities (PSD) of the streamwise and the cross-stream velocities is performed (The DMD mode corresponding to the time-averaged flow is not included). The PSDs are obtained using the fast Fourier transformation combined with Welch's method (Welch 1967). For the PSD analysis of the velocity signals, the time series of u and v at 17 streamwise locations shown in Fig. 13 are sampled with a sampling frequency of $\Delta tU_\infty/D = 0.01$. The time span of the sampling is $TU_\infty/D = 300$. The spanwise-averaged PSDs of u and v are shown in Fig. 14. At $x/D = 0.2$ and $y/D = 1.4\tilde{}2.0$, a dominant frequency of is shown at $f_{KH}D/U_\infty = 0.45\tilde{}0.5$ and this dominant frequency is related to the Kelvin-Helmholtz (KH) instability of the shear layer. The value of the frequency is slightly larger than the previous published data of $f_{KH}D/U_\infty = 0.35$ in Abdalla et al. (2007) at $Re = 4500$ and $f_{KH}D/U_\infty = 0.42$ in Gu et al. (2017) at $Re = 3000$, which may be due to the higher investigated Re for the present study. The predicted value of the KH instability frequency is also close to the value of $f_{KH}D/U_\infty = 0.59$ reported in Mercier et al. (2020) at $Re = 2.5 \times 10^5$. In addition, at these streamwise locations, the frequency peaks at $2f_{KH}D/U_\infty$ related to secondary harmonic are also observed. It worth mentioning that there are frequency peaks at $f_sD/U_\infty = 0.25$ for u and v at the locations of $(x/D, y/D) = (2, 1.2)$ and $(x/D, y/D) = (4, 1.6)$, which is the subharmonic of the primary KH instability frequency. According to Gu et al. (2017), this subharmonic is related to the vortex pairing. Furthermore, the widely reported low-frequency mode in Abdalla et al. (2007), Gu et al. (2017, 2018) and Wu et al. (2020) can be also seen at $f_mD/U_\infty = 0.05\tilde{}0.09$ for v at $x/D = 4$ and $y/D = 0.4, 0.8$ and 1.2. However, this low-frequency mode is not obvious which may be due to the wide range of low frequencies related to the characteristics of fully developed turbulence. A comparison between the DMD spectrum and the power spectral densities (PSD) of the streamwise and the cross-stream velocities at $x/D = 1, 2, 4$ and $y/D = 1.6$ with different

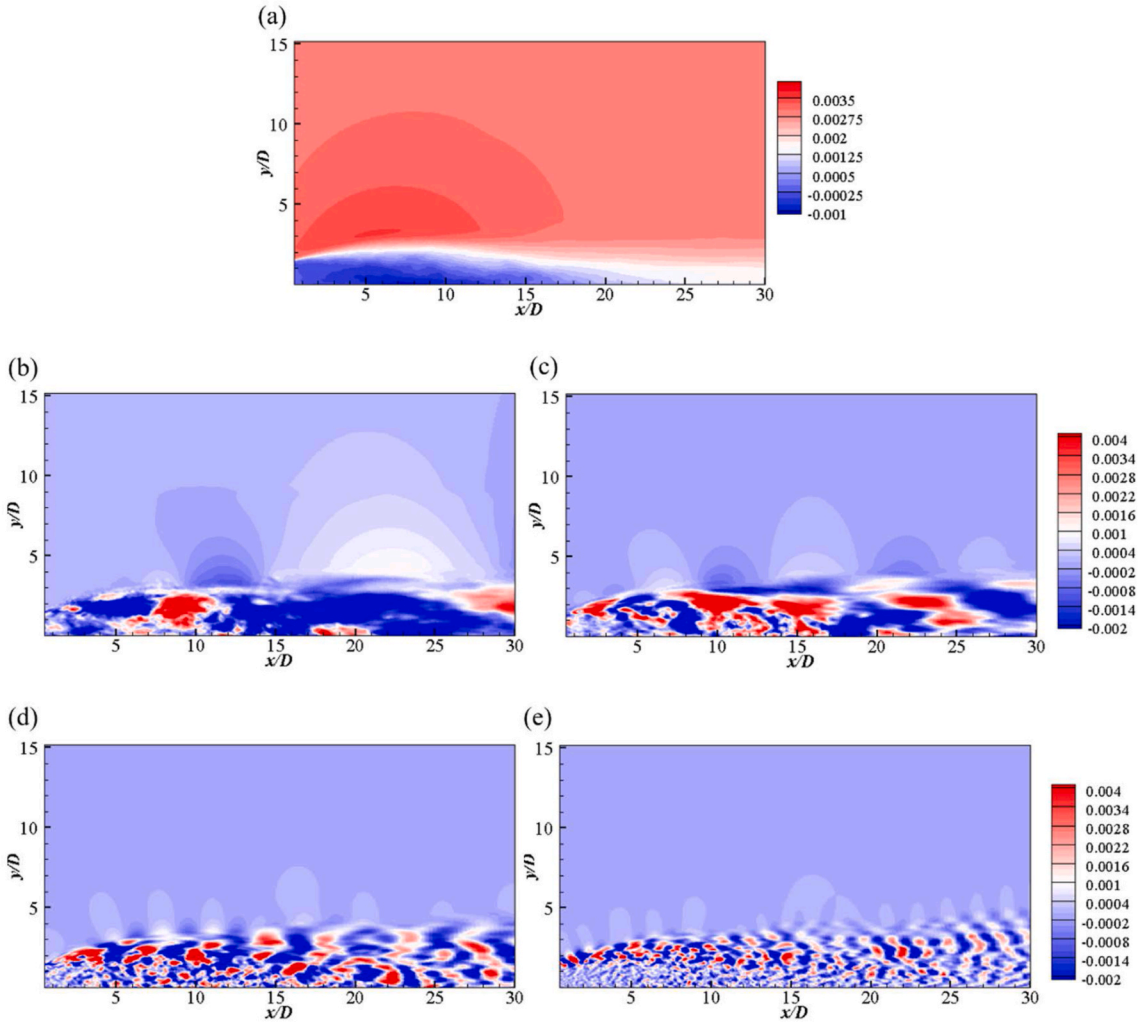

Fig. 17. The contours of the nondimensionalized streamwise velocity u/U_∞ corresponding to the DMD modes marked in Fig. 11: (a) Mode 0; (b) Mode 1; (c) Mode 2; (d) Mode 3; (e) Mode 4.

heights is shown in Fig. 15 (The DMD mode corresponding to the time-averaged flow is not included). The frequencies obtained by $\mathrm{Im}(\log(\mu_i)/\Delta t)$ are divided by 2π to compare with the PSD. It can be seen that the four clusters (indicated by the grey vertical stripes) of the DMD modes can correspond well to the different frequency peaks in PSD. Therefore, it can be inferred that Modes 3 and 4 corresponds to sub-harmonic and primary KH modes, respectively. Modes 1 and 2 can correspond to the low-frequency motions. As mentioned in Taira et al. (2017), DMD can be viewed as a combination of POD and the Fourier transformation; hence, the DMD modes can capture both the spatial coherency and temporal evolution of the flow structures while Fourier transformation can only obtain the characteristic frequencies of the velocity signals at a single point in the flow field.

The contours of the streamwise velocity corresponding to the DMD modes denoted as Modes 0–4 in Fig. 11 from the 4 clusters are shown in Fig. 17 (a)~(e). As has been mentioned, the mode with 0 frequency denotes the time-averaged flow which is similar to that shown in Fig. 9 (The contour levels are different because all the DMD modes obtained by (22) are normalized). The contours of the streamwise velocity of the mode with the second peak (marked with Mode 1) show that a large-scale structure appears with a pair of high- and low-speed regions with the size relative to the cross-stream size of the wake region. The structures of the third mode (marked with Mode 2) shows smaller streamwise wavelength. With the increasing frequency and decreasing amplitude of the higher order modes, the structures are becoming smaller and the energetic regions are located closer to the shear layer of the recirculation region behind the square while more weak fluctuations are distributed near the bottom wall.

Finally, a reduced-order model (ROM) of the flow field is built based on the DMD modes together with their corresponding amplitudes and frequencies obtained by the SPDMD algorithm. To achieve this, the velocity at a point (x,y) at $t=t_n$ is reconstructed by

$$u(x,y,t_n)=\sum_{i=1}^{N_{sp}}\alpha_i\varphi_i(x,y)\mu_i^{n-1} \tag{25}$$

where $\varphi_i(x,y)$ denotes the value at (x,y) of the ith mode and α_i is its amplitude calculated by the SPDMD method (Jovanović et al., 2014). N_{sp} is the total number of DMD modes used to build the ROM.

The ROMs of a flow field at low Re are usually built by $N_{sp}\sim \mathrm{O}(10)$ modes. However due to multi-scale features of the fully developed turbulent flow in the present study, a relatively larger number of DMD modes are required. To examine the influence of the number of modes used to build the ROM, the time histories of the streamwise velocities at 6 locations of $(x/D,y/D)=(0.5,0.5),\ (1,0.5),(1.5,0.5),(2,0.5),\ (3,0.5),\ (4,0.5)$ behind the square obtained by (23) using $N_{sp}=57$ and 103 modes are compared with the original numerical simulation data. For $N_{sp}=57$, large discrepancy is observed near the square at $(x/D,y/D)=(0.5,0.5)$

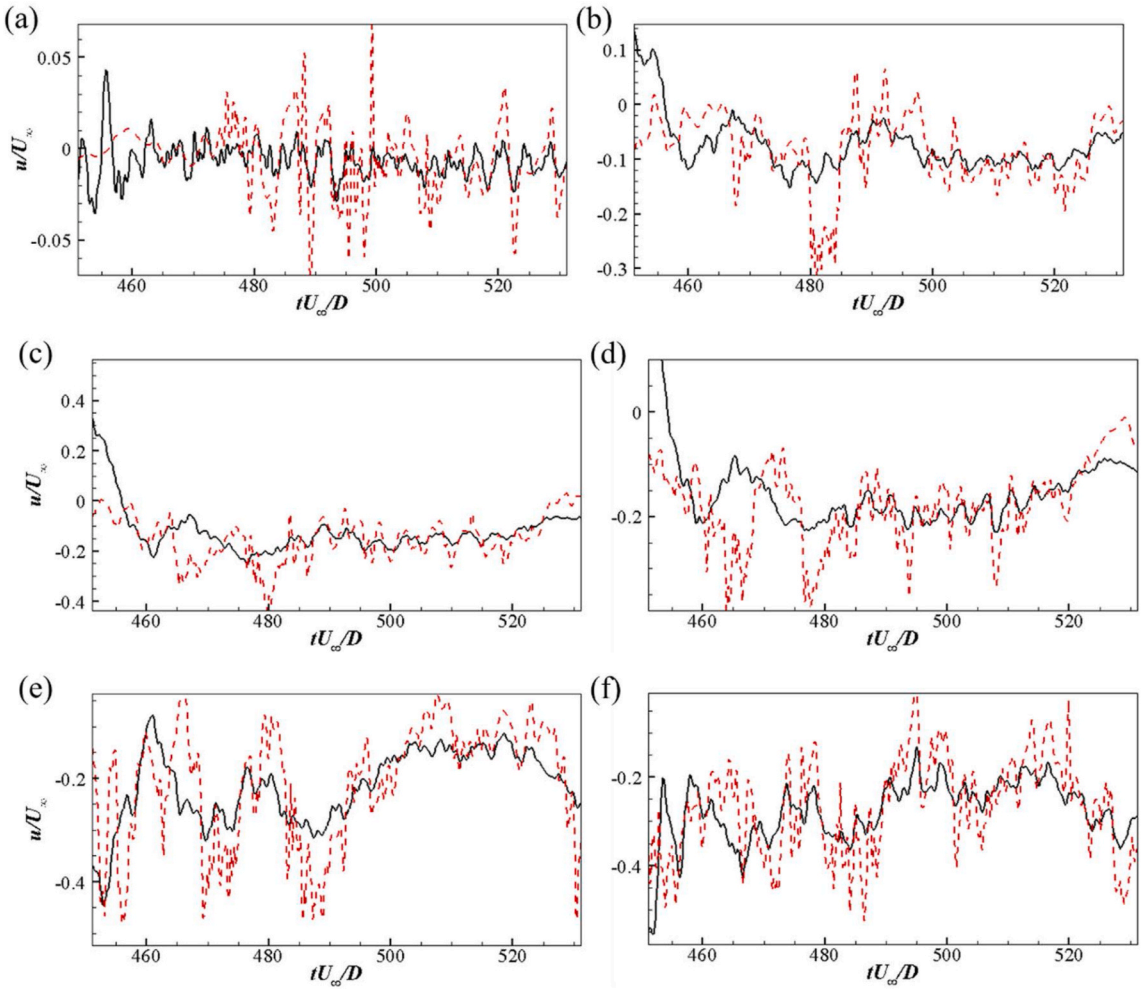

Fig. 18. Time histories of the streamwise velocity given by ROMs (Eq. (18)) (solid) with N_{sp} = 57modes and the simulation results (red dashes) at different $(x/D, y/D)$ of (a) $(0.5, 0.5)$; (b) $(1, 0.5)$; (c)$(1.5, 0.5)$; (d) $(2, 0.5)$; (e) $(3, 0.5)$; (f)$(4, 0.5)$. (For interpretation of the references to color in this figure legend, the reader is referred to the Web version of this article.)

indicating that more small-scale structures are generated, and more modes are needed to capture the dynamical behaviors. At $(x/D, y/D) = (3, 0.5)$, $(4, 0.5)$, the time variations of the streamwise velocity can be better predicted by the ROM despite that the amplitudes of the ROM are lower than the simulation results. When increasing the modes number to $N_{sp} = 103$, the ROM results become more accurate. It is worth mentioned that the ROM built by using these DMD modes only captures temporal evolution of large-scale turbulent structures. The production of small-scale turbulent structures which lead to the spikes of the time histories of the streamwise velocity shown in Figs. 18 and 19 can be captured by including even more DMD modes, which are truncated in the present ROM.

5. Conclusion

Three-dimensional Spalart-Allmaras Delayed Detached Eddy Simulations of the flow around a wall-mounted square structure are carried out. The Reynolds number based on the free stream velocity and the structure height (D) is $Re = 1.19 \times 10^5$. The drag coefficients as well as the time- and spanwise-averaged streamwise velocity profiles are in a reasonable agreement with the published data. Systematical analysis is presented in terms of the hydrodynamic quantities, Reynolds-averaged statistics and the instantaneous vortical structures. Furthermore, Dynamic Mode Decomposition has been applied to the (u, v) data in the 2D XY-plane at the mid-span point of the flow field, which can extract the dynamic information of the coherent structures in the wake region behind the square structures. The main conclusions can be outlined as follows:

1. The frequency of the time history of the lift coefficient C_L is lower than that of the drag coefficient C_D. The instantaneous C_L is approximately associated with C_D.
2. Three main time-averaged recirculation motions are observed around the square. A small one appears around the front face of the structure and a large recirculation motion formed behind the square. A small vortex is induced by the large recirculation motion around the rear face of the structure.
3. The shear layer sheds from the square and rolls up into small-scale hairpin structures. Further downstream, the small-scale vortical structures around the shear layer are in the spanwise direction while in the wake region, they are tilted in the streamwise direction.
4. The frequencies and amplitudes of the dominant DMD modes which contribute the most to the inherent dynamics are obtained through the sparsity-promoted DMD algorithm. Even though the flow under investigation is fully turbulence at a high Reynolds number, it can still be reconstructed by a finite number of DMD modes.

CRediT authorship contribution statement

Guang Yin: Conceptualization, Methodology, Software, Validation, Formal analysis, Investigation, Writing - original draft, Writing - review

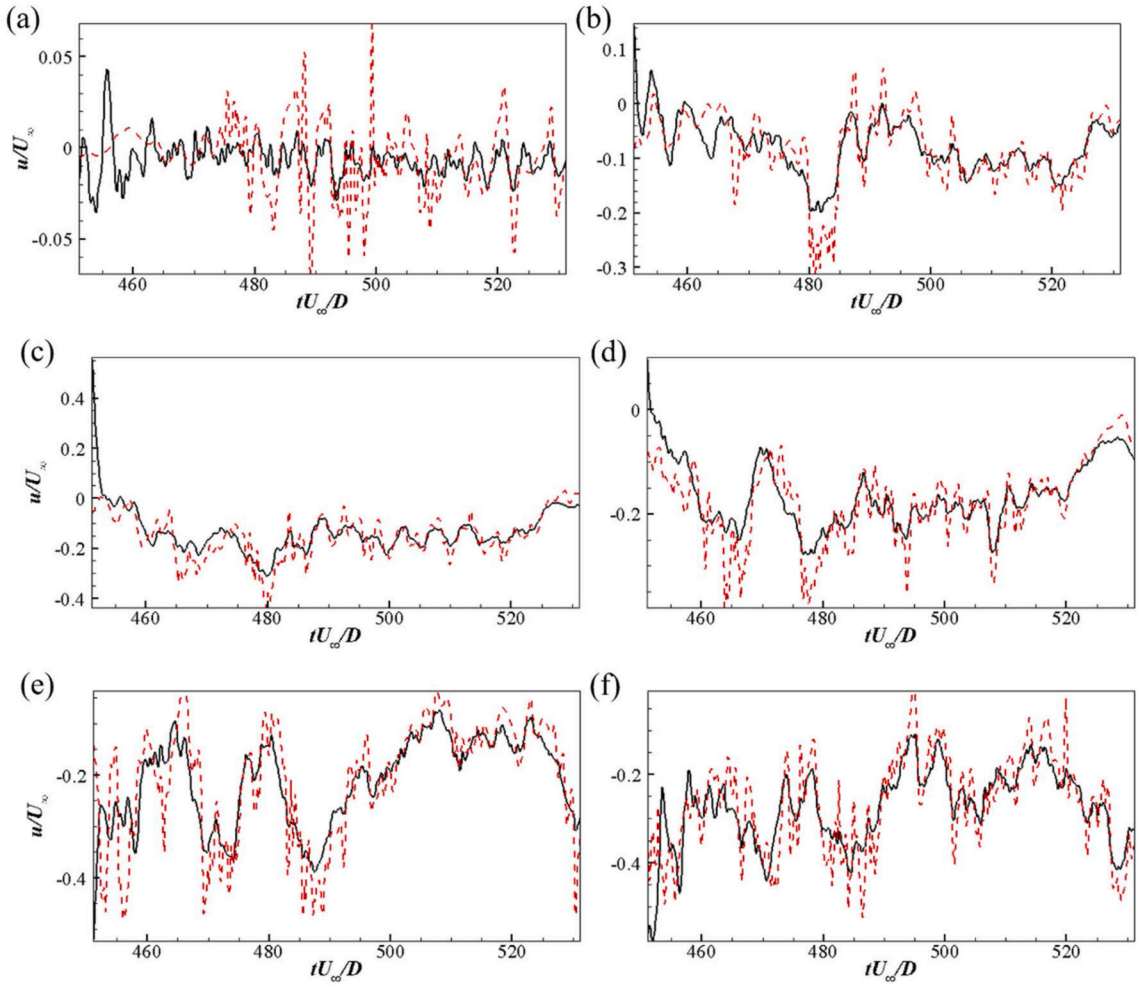

Fig. 19. Time histories of the streamwise velocity given by ROMs (Eq. (18)) with $N_{sp} = 103$modes and the simulation results (red dashes) at different $(x/D, y/D)$ of (a) $(0.5, 0.5)$; (b) $(1, 0.5)$; (c)$(1.5, 0.5)$; (d) $(2, 0.5)$; (e) $(3, 0.5)$; (f)$(4, 0.5)$. (For interpretation of the references to color in this figure legend, the reader is referred to the Web version of this article.)

& editing, Visualization. **Muk Chen Ong:** Conceptualization, Investigation, Writing - review & editing, Resources, Supervision, Project administration, Funding acquisition.

Declaration of competing interest

The authors declare that they have no known competing financial interests or personal relationships that could have appeared to influence the work reported in this paper.

Acknowledgement

This study was supported with computational resources provided by the Norwegian Metacenter for Computational Science (NOTUR), under Project No: NN9372K.

References

Abdalla, I.E., Cook, M.J., Yang, Z., 2007. Numerical study of transitional separated–reattached flow over surface-mounted obstacles using large-eddy simulation. Int. J. Numer. Methods Fluid. 54 (2), 175–206.

Acharya, S., Dutta, S., Myrum, T.A., Baker, R.S., 1994. Turbulent flow past a surface-mounted two-dimensional rib. J. Fluid Eng. 116 (2), 238–246.

Arie, M., kiya, M., Tamura, H., Kosugi, M., Takaoka, K., 1975. Flow over rectangular cylinders immersed in a turbulent boundary layer: Part 2 flow patterns and pressure distributions. Bulletin of JSME 18 (125), 1269–1276.

Bagheri, S., 2013. Koopman-mode decomposition of the cylinder wake. J. Fluid Mech. 726, 596–623.

Bergeles, G., Athanassiadis, N., 1983. The flow past a surface-mounted obstacle. J. Fluid Eng. 105 (4), 461–463.

Boudreau, M., Dumas, G., Veilleux, J.C., 2017. Assessing the ability of the DDES turbulence modeling approach to simulate the wake of a bluff body. Aerospace 4 (3), 41.

Crabb, D., Durao, D.F.G., Whitelaw, J.H., 1977. Velocity characteristics in the vicinity of a two-dimensional rib. In: Proceeding of the 4th Brazilian Congress on Mechanical Engeering, Florianopolis, Brazil, pp. 47–58.

Dai, Y., Wang, H., Tian, C., 2017. Numerical simulations of turbulent flow over two surface-mounted tandem square cylinders. In: ASME 2017 36th International Conference on Ocean, Offshore and Arctic Engineering. American Society of Mechanical Engineers Digital Collection.

Gu, H., Yang, J., Liu, M., 2017. Study on the instability in separating–reattaching flow over a surface-mounted rib. Int. J. Comput. Fluid Dynam. 31 (2), 109–121.

Gu, H., Yao, M., Zhao, P., Li, X., Liu, M., 2018. Numerical simulation of manipulated flow and heat transfer over surface-mounted rib. Int. J. Therm. Sci. 129, 124–134.

He, G., Wang, J., Pan, C., 2013. Initial growth of a disturbance in a boundary layer influenced by a circular cylinder wake. J. Fluid Mech. 718, 116–130.

Hemmati, A., Wood, D.H., Martinuzzi, R.J., 2019. Wake dynamics and surface pressure variations on two-dimensional normal flat plates. AIP Adv. 9 (4), 045209.

Hwang, R.R., Chow, Y.C., Peng, Y.F., 1999. Numerical study of turbulent flow over two-dimensional surface-mounted ribs in a channel. Int. J. Numer. Methods Fluid. 31 (4), 767–785.

Jovanović, M.R., Schmid, P.J., Nichols, J.W., 2014. Sparsity-promoting dynamic mode decomposition. Phys. Fluids 26 (2), 024103.

Li, Z., Prsic, M.A., Ong, M.C., Khoo, B.C., 2018. Large Eddy Simulations of flow around two circular cylinders in tandem in the vicinity of a plane wall at small gap ratios. J. Fluid Struct. 76, 251–271.

Liu, Y.Z., Ke, F., Sung, H.J., 2008. Unsteady separated and reattaching turbulent flow over a two-dimensional square rib. J. Fluid Struct. 24 (3), 366–381.

Lumley, J.L., 2007. Stochastic Tools in Turbulence. Courier Corporation.
Martinuzzi, R., Tropea, C., 1993. The flow around surface-mounted, prismatic obstacles placed in a fully developed channel flow. Transactions-American Society of Mechanical Engineers Journal of Fluids Engineering 115, 85-85.
Mercier, P., Ikhennicheu, M., Guillou, S., Germain, G., Poizot, E., Grondeau, M., et al., 2020. The merging of Kelvin–Helmholtz vortices into large coherent flow structures in a high Reynolds number flow past a wall-mounted square cylinder. Ocean Eng. 204, 107274.
Najjar, F.M., Balachandar, S., 1998. Low-frequency unsteadiness in the wake of a normal flat plate. J. Fluid Mech. 370, 101–147.
Ohmichi, Y., 2017. Preconditioned dynamic mode decomposition and mode selection algorithms for large datasets using incremental proper orthogonal decomposition. AIP Adv. 7 (7), 075318.
Ong, M.C., Utnes, T., Holmedal, L.E., Myrhaug, D., Pettersen, B., 2009. Numerical simulation of flow around a smooth circular cylinder at very high Reynolds numbers. Mar. Struct. 22 (2), 142–153.
Ong, M.C., Utnes, T., Holmedal, L.E., Myrhaug, D., Pettersen, B., 2010. Numerical simulation of flow around a circular cylinder close to a flat seabed at high Reynolds numbers using a k–ε model. Coast Eng. 57 (10), 931–947.
Ong, M.C., Trygsland, E., Myrhaug, D., 2017. Numerical study of seabed boundary layer flow around monopile and gravity-based wind turbine foundations. J. Offshore Mech. Arctic Eng. 139 (4), 042001.
Pan, C., Xue, D., Wang, J., 2015. On the accuracy of dynamic mode decomposition in estimating instability of wave packet. Exp. Fluid 56 (8), 164.
Prsic, M.A., Ong, M.C., Pettersen, B., Myrhaug, D., 2019. Large Eddy simulations of flow around tandem circular cylinders in the vicinity of a plane wall. J. Mar. Sci. Technol. 24 (2), 338–358.
Rowley, C.W., Mezić, I., Bagheri, S., Schlatter, P., Henningson, D.S., 2009. Spectral analysis of nonlinear flows. J. Fluid Mech. 641, 115–127.
Rumsey, C.L., Allison, D.O., Biedron, R.T., Buning, P.G., Gainer, T.G., Morrison, J.H., et al., 2001. CFD Sensitivity Analysis of a Modern Civil Transport Near Buffet-Onset Conditions.
Ryu, D.N., Choi, D.H., Patel, V.C., 2007. Analysis of turbulent flow in channels roughened by two-dimensional ribs and three-dimensional blocks. Part I: Resistance. Int. J. Heat Fluid Flow 28 (5), 1098–1111.
Santiago, J.L., Martilli, A., Martín, F., 2007. CFD simulation of airflow over a regular array of cubes. Part I: three-dimensional simulation of the flow and validation with wind-tunnel measurements. Boundary-Layer Meteorol. 122 (3), 609–634.
Schmid, P.J., 2010. Dynamic mode decomposition of numerical and experimental data. J. Fluid Mech. 656, 5–28.
Schmid, P.J., 2011. Application of the dynamic mode decomposition to experimental data. Exp. Fluid 50 (4), 1123–1130.
Schmid, P.J., Li, L., Juniper, M.P., Pust, O., 2011. Applications of the dynamic mode decomposition. Theor. Comput. Fluid Dynam. 25 (1–4), 249–259.
Schmid, P.J., Violato, D., Scarano, F., 2012. Decomposition of time-resolved tomographic PIV. Exp. Fluid 52 (6), 1567–1579.
Seena, A., Sung, H.J., 2011. Dynamic mode decomposition of turbulent cavity flows for self-sustained oscillations. Int. J. Heat Fluid Flow 32 (6), 1098–1110.
Seena, A., Sung, H.J., 2013. Spatiotemporal representation of the dynamic modes in turbulent cavity flows. Int. J. Heat Fluid Flow 44, 1–13.
Spalart, P.R., 1997. Comments on the feasibility of LES for wings, and on a hybrid RANS/LES approach. In: Proceedings of First AFOSR International Conference on DNS/LES. Greyden Press.
Spalart, P.R., Deck, S., Shur, M.L., Squires, K.D., Strelets, M.K., Travin, A., 2006. A new version of detached-eddy simulation, resistant to ambiguous grid densities. Theor. Comput. Fluid Dynam. 20 (3), 181.
Spalding, D.B., 1961. A single formula for the "law of the wall". J. Appl. Mech. 28 (3), 455–458.
Statnikov, V., Sayadi, T., Meinke, M., Schmid, P., Schröder, W., 2015. Analysis of pressure perturbation sources on a generic space launcher after-body in supersonic flow using zonal turbulence modeling and dynamic mode decomposition. Phys. Fluids 27 (1), 016103.
Schlünzen, K.H., Bächlin, W., Brünger, H., Eichhorn, J., Grawe, D., Schenk, R., Winkler, C., 2004. June. An evaluation guideline for prognostic microscale wind field models. In: 9th International Conference on Harmonisation within Atmospheric Dispersion Modelling for Regulatory Purposes, pp. 1–4.
Taira, K., Brunton, S.L., Dawson, S.T., Rowley, C.W., Colonius, T., McKeon, B.J., et al., 2017. Modal analysis of fluid flows: an overview. AIAA J. 55 (12), 4013–4041.
Tariq, A., Panigrahi, P.K., Muralidhar, K., 2004. Flow and heat transfer in the wake of a surface-mounted rib with a slit. Exp. Fluid 37 (5), 701–719.
Tauqeer, M.A., Li, Z., Ong, M.C., 2017. Numerical simulation of flow around different wall-mounted structures. Ships Offshore Struct. 12 (8), 1109–1116.
Tropea, C.D., Gackstatter, R., 1985. The flow over two-dimensional surface-mounted obstacles at low Reynolds numbers. J. Fluid Eng. 107 (4), 489–494.
Tian, X., Ong, M.C., Yang, J., Myrhaug, D., 2014. Large-eddy simulation of the flow normal to a flat plate including corner effects at a high Reynolds number. J. Fluid Struct. 49, 149–169.
Tian, X., Ong, M.C., Yang, J., Myrhaug, D., 2016. Large-eddy simulations of flow normal to a circular disk at Re$= 1.5\times 10^5$. Comput. Fluids 140, 422–434.
Tissot, G., Cordier, L., Benard, N., Noack, B.R., 2013. Dynamic mode decomposition of PIV measurements for cylinder wake flow in turbulent regime. In: TSFP Digital Library Online. Begel House Inc.
Tissot, G., Cordier, L., Benard, N., Noack, B.R., 2014. Model reduction using dynamic mode decomposition. Compt. Rendus Mec. 342 (6–7), 410–416.
Tu, J., Rowley, C., Aram, E., Mittal, R., 2011. Koopman spectral analysis of separated flow over a finite-thickness flat plate with elliptical leading edge. In: 49th AIAA Aerospace Sciences Meeting Including the New Horizons Forum and Aerospace Exposition, p. 38.
Welch, P., 1967. The use of fast Fourier transform for the estimation of power spectra: a method based on time averaging over short, modified periodograms. IEEE Trans. Audio Electroacoust. 15 (2), 70–73.
Wu, W., Meneveau, C., Mittal, R., 2020. Spatio-temporal dynamics of turbulent separation bubbles. J. Fluid Mech. 883.
Young, D.L., Eldho, T.I., Chang, J.T., 2006. Large eddy simulation of turbulent flows in external flow field using three-step FEM–BEM model. Eng. Anal. Bound. Elem. 30 (7), 564–576.
Zhang, Y., Cattafesta, L., Ukeiley, L., 2017. Identification of coherent structures in cavity flows using stochastic estimation and dynamic mode decomposition. In: 10th International Symposium on Turbulence and Shear Flow Phenomena (TSFP10). Chicago, USA.(A) TR-PIV, Mode Shape of U.